Final Research Report

Project Title:	Room Temperature Hydrogen Storage in Nano-Confined Liquids
Project Period:	March 5, 2012 to March 14, 2014
Submission Date:	June 12, 2014
Recipient:	HRL Laboratories, LLC 3011 Malibu Canyon Road Malibu, California 90265
Website	www.hrl.com
Award Number:	DE-EE0005659

PI: John J. Vajo
Senior Research Scientist
Phone: 310-317-5745
Email: jjvajo@hrl.com

Submitted by: Lynn Jones
Contracts Manager
Phone: 310-317-5652
Email: HRLLabsContracts@hrl.com

DOE Project Team:

DOE Contracting Officer - Christina Kouch
(720) 356-1674
Christina.Kouch@go.doe.gov

DOE Project Manager (GO) - Katie Randolph
(720) 356-1759
Katie.Randolph@go.doe.gov

Executive Summary: DOE continues to seek solid-state hydrogen storage materials with hydrogen densities of ≥6 wt% and ≥50 g/L that can deliver hydrogen and be recharged at room temperature and moderate pressures enabling widespread use in transportation applications. Meanwhile, development including vehicle engineering and delivery infrastructure continues for compressed-gas hydrogen storage systems. Although compressed gas storage avoids the materials-based issues associated with solid-state storage, achieving acceptable volumetric densities has been a persistent challenge. This project examined the possibility of developing storage materials that would be compatible with compressed gas storage technology based on enhanced hydrogen solubility in nano-confined liquid solvents. These materials would store hydrogen in molecular form eliminating many limitations of current solid-state materials while increasing the volumetric capacity of compressed hydrogen storage vessels.

Experimental methods were developed to study hydrogen solubility in nano-confined liquids. These methods included 1) fabrication of composites comprised of volatile liquid solvents for hydrogen confined within the nano-sized pore volume of nanoporous scaffolds and 2) measuring the hydrogen uptake capacity of these composites without altering the composite composition. The hydrogen storage capacities of these nano-confined solvent/scaffold composites were compared with bulk solvents and with empty scaffolds. The solvents and scaffolds were varied to optimize the enhancement in hydrogen solubility that accompanies confinement of the solvent. In addition, computational simulations were performed to study the molecular-scale structure of liquid solvent when confined within an atomically realistic nano-sized pore of a model scaffold. Confined solvent was compared with similar simulations of bulk solvent. The results from the simulations were used to formulate a mechanism for the enhanced solubility and to guide the experiments.

Overall, the combined experimental measurements and simulations indicate that hydrogen storage based on enhanced solubility in nano-confined liquids is unlikely to meet the storage densities required for practical use. Only low gravimetric capacities of < 0.5 wt% were achieved. More importantly, solvent filled scaffolds had lower volumetric capacities than corresponding empty scaffolds.

Nevertheless, several of the composites measured did show significant (>~ 5x) enhanced hydrogen solubility relative to bulk solvent solubility, when the hydrogen capacity was attributed only to dissolution in the confined solvent. However, when the hydrogen capacity was compared to an empty scaffold that is known to store hydrogen by surface adsorption on the scaffold walls, including the solvent always reduced the hydrogen capacity. For the best composites, this reduction relative to an empty scaffold was ~30%; for the worst it was ~90%. The highest capacities were obtained with the largest solvent molecules and with scaffolds containing 3-dimensionally confined pore geometries. The simulations suggested that the capacity of the composites originated from hydrogen adsorption on the scaffold pore walls at sites not occupied by solvent molecules. Although liquid solvent filled the pores, not all of the adsorption sites on the pore walls were occupied due to restricted motion of the solvent molecules within the confined pore space.

1. Project Goal and Objectives: The overall goal of this project was the development of hydrogen storage materials with (material basis) hydrogen densities of ≥6 wt% and 50 g/L at near room temperature and <350 bar that would be compatible with the vehicle engineering and delivery infrastructure currently being developed for compressed gas storage.

The objectives of this project were 1) to measure the enhanced hydrogen storage capacity of liquid solvents when they are confined within the pore volume of nanoporous scaffolds; 2) to validate and understand the measured storage capacities using computations and simulations; 3) to optimize the scaffold and liquid to maximize the storage capacity; and 4) to minimize the vapor content of the discharged hydrogen.

The expected outcomes were 1) accurate measurements of the solubility enhancement for nano-confined liquids; 2) an understanding of the mechanism of enhancement; and 3) an assessment of the possibility for hydrogen storage via enhanced solubility to meet the DOE goals.

2. Outcomes: The goal of developing hydrogen storage materials with hydrogen densities of ≥6 wt% and 50 g/L at near room temperature and <350 bar was not achieved. However, accurate measurements of the enhanced hydrogen storage capacities of liquid solvents confined within the pore volume of nanoporous scaffolds were successfully made (Objective 1). Furthermore, molecular level simulations of confined solvents were performed and led to a preliminary understanding of the enhancement mechanism (Objective 2) and together with the measurements, some optimization of the storage capacity was achieved (Objective 3). Objective 4 was not pursued. Most significantly, the results enabled a confident assessment indicating that hydrogen storage materials based on enhanced solubility in liquid solvents confined within nanoporous scaffolds are unlikely to meet the DOE hydrogen storage goals.

3. Background: The prospect of storing hydrogen by dissolving molecular H_2 gas in a liquid solvent is compelling because the dissolution is chemically simple, readily reversible, and can occur relatively fast at room temperature with low enthalpy. This approach could significantly improve the capacity of compressed hydrogen systems with minimal changes to developing compressed gas vehicle designs and delivery infrastructure, thus facilitating technology transition. Despite these attractive attributes, the dissolution (solubility) of hydrogen in bulk liquids is much too low to be technologically useful. For example, hexane, which has a relatively high hydrogen solubility, dissolves <0.2 wt% H_2 at room temperature and 100 bar.[1] Even at hydrogen pressures as high as 700 bar (10,000 psi), the solubility is <1 wt%. These solubilities are at least 10x too low for practical storage applications.

Recently, however, the solubility of gases in liquids confined within the pore volumes of nanoporous scaffolds has been studied by Professor Marc Pera-Titus and coworkers at the Institut de Recherches sur la Catalyse et l'Environnement de Lyon (IRCELYON), CNRS – Université de Claude Bernard Lyon, Villeurbanne Cedex, France. They report enhanced solubilities for different gases in several different solvent liquids that are confined within nanoporous silica or alumina solids. (2, 3, 4) The enhancements, relative to the solubility in the bulk liquid, range from ~2x to >50x. The gases include H_2, CH_4, and C_2H_6; the liquids include CCl_4, H_2O, ethanol, and hexane; and the scaffolds include nanoporous alumina, MCM-41, and silica gel. In particular, a 16x enhancement was reported for H_2 in hexane confined within MCM-41 with 3.4 nm pores while a 50x enhancement was claimed for H_2 dissolved in

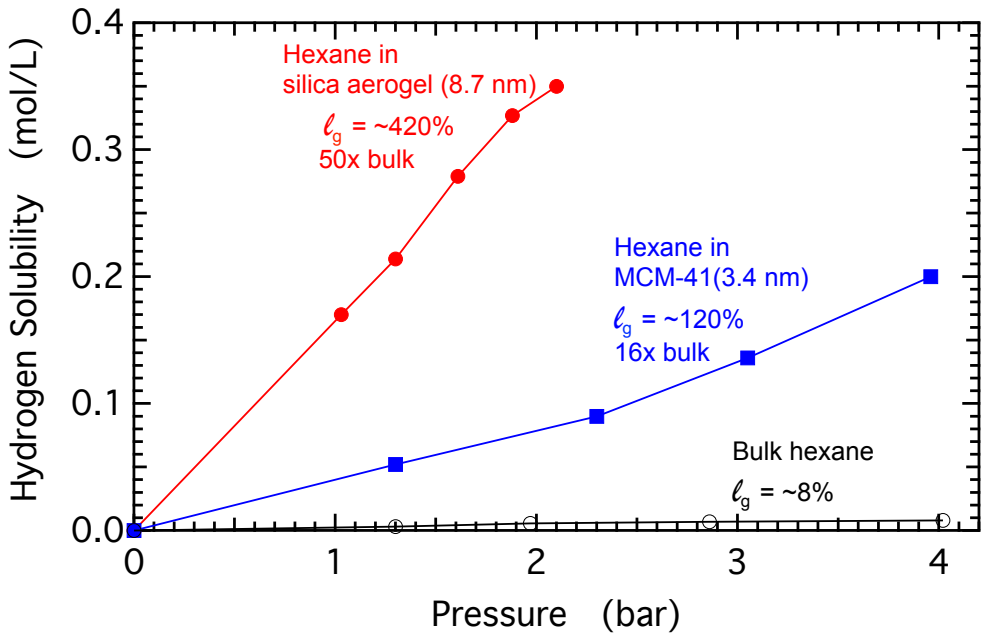

Figure 1. Enhanced solubility of hydrogen in nano-confined hexane obtained from data in Ref. 2. Hydrogen solubility (mol/L) versus pressure (bar) in bulk hexane (open circles, black) and hexane confined in MCM-41 (filled squares, blue) and silica aerogel (filled circles, red).

hexane within silica gel with 8.7 nm pores. Representative data from Ref. 2 is shown in Figure 1. The solubility curves are linear indicating that Henry's law is obeyed as expected. The slope of the line gives the solubility coefficient. For hydrogen dissolving in hexane that is contained (confined) within the pores of MCM-41 the slope is 16x greater than for bulk hexane. For hexane in silica aerogel, the reported slope is ~50x greater.

In addition to these relative enhancements, the absolute solubilities given in terms of percent (%) were ~120% for hexane/MCM-41 and 420% for hexane/silica aerogel. Importantly, both solubilities were >100%. In the form of percent (%), the gas solubility refers to the volumetric density of gas in the liquid relative to the density of the gas phase in equilibrium with the liquid. Thus, a solubility of 50% means that the density of gas in the liquid is ½ (or 50%) of the density in the gas. A solubility of 100% means equal densities, while >100% means that the gas density within the liquid is actually greater than the density of the pure gas. Compared to a pure compressed gas tank, a solubility of >100% is required for hydrogen storage; otherwise the volumetric density would be decreased by using the liquid. We note that gravimetrically, using a solvent always reduces the gravimetric density because without counting the weight of a tank, compressed gas is by definition 100 wt%.

The enhanced solubilities reported are sufficiently high to be interesting for practical applications. For example, if we assume a hydrogen solubility in nanoconfined hexane of ~20x the bulk solubility, which is equal to an absolute solubility of 200% (within the range given above) and that this solubility can be achieved at 350 bar, then a solubility of 29 mol/L would be attained in the liquid phase. This is a big assumption because the reported 120% and 420% solubilities were measured at only ~5 bar and it is not known how the solubility will scale with pressure over such large range, from 5 to 350 bar. Nevertheless, if we further assume that this solubility can be attained using a scaffold with a pore volume of 4 cm^3/g, then using a liquid density of 0.66 g/cm^3 (i.e., hexane) and a scaffold skeletal density of 2.1 g/cm^3 (i.e., typical for porous carbon) gives capacities for the nano-confined hexane/carbon scaffold composite of 6

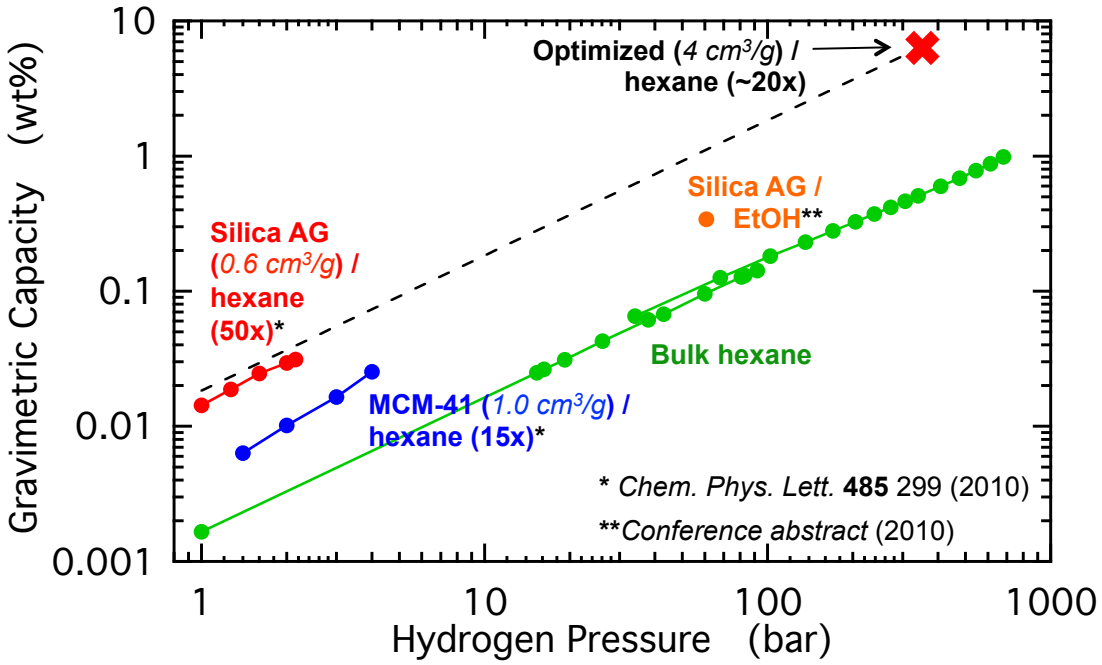

Figure 2. Projection of hydrogen storage capacity based on enhanced solubility in nano-confined hexane. The solubility of hydrogen in bulk hexane obeys Henry's law up to nearly 1000 bar but even without accounting for the weight of a containment vessel, the solubility is ~10x too low for practical hydrogen storage. Data for hexane in MCM-41 is 15x the bulk but MCM-41 has a low pore volume of 1.0 cm^3/g and so falls below the projection line required for the DOE targets. Data for hexane in silica aerogel is 50x the bulk and so even with a low pore volume of 0.6 cm^3/g, it is only slight below the projection. Assuming a more moderate enhancement of 20x with an optimized scaffold of 4 cm^3/g and Henry's law behavior up to 350 bar enables a storage capacity of 6 wt%.

wt% and 50 g/L. A pore volume of 4 cm^3/g is very high but has been demonstrated. This projection is shown in Figure 2.

4. Accomplishment — measurement of hydrogen solubility in nano-confined liquids: The main objective of this project was to measure the effect of nano-confinement on the solubility of hydrogen in liquid solvents, such as hexane. To meet this objective, accurate measurements of hydrogen solubility in both bulk solvents and nano-confined solvents were required. Solubility measurements of gases in liquids, including hydrogen in hexane, have been made for more than 100 years by a variety of techniques including volumetric methods. While these techniques have been optimized for bulk liquid samples, most would not also work well for samples where the liquid is confined within the pore volume of a nanoporous scaffold. These scaffolds are often dry powders or granules, such as zeolites or activated carbons, which can retain their dry character even when the pores are completely or nearly completely filled with liquid.

As an example, we consider a typical volumetric method. These volumetric methods usually include a thorough degassing step, to remove previously dissolved gases such as air, by stirring the liquid while under dynamic vacuum. The liquid evaporates together with dissolved gases and eventually the dissolved gases are depleted. Then the liquid is equilibrated with the desired gas at a chosen pressure, again by stirring. A known aliquot of the gas-saturated liquid is then withdrawn from the sample and equilibrated at a much lower pressure by further stirring. At this point the amount of gas that desorbed from the aliquot is determined from the final gas pressure

in equilibrium with the liquid in a calibrated volume; a correction is applied for the liquid vapor pressure while any gas remaining dissolved is considered negligible. This procedure is not readily applicable to nano-confined liquid/scaffold composites for several reasons. Specifically, in order to facilitate gas moving into or out of the liquid phase, most of the steps involve stirring, which is not easily performed on solid samples. Moreover, even if confined liquid/scaffold composite solids could be stirred, it is uncertain that the desired agitation would be transmitted to the incorporated liquid phase. In addition, the degasing procedure involves loss of an unknown amount of solvent. While this loss is not important if only an aliquot of the liquid is subsequently used (as described above), this loss is unacceptable if a particular solvent loading of the scaffold is being tested.

Thus, we developed volumetric measurement-based experimental protocols for determining hydrogen capacity (solubility) of volatile liquid samples applicable to both bulk liquids and confined-liquid/scaffold composites. These procedures address the issues of degassing without solvent loss, agitation to facilitate equilibration, and corrections due to solvent vapor pressure. These techniques were then used to measure the solubility of hydrogen in bulk hexane from ~10 bar to 70 bar.

4.1 Degassing procedure: Accurate measurements of the solubility of gases in liquids require beginning with thoroughly degased liquid samples. The following procedure was developed to minimize solvent loss while also being applicable to confined liquid samples.

The scheme uses freeze-pump-thaw cycles with liquid nitrogen at 77 K. To initially remove condensable gases such as N_2, O_2, H_2O, Ar, and CO_2, that might be retained at 77 K, solvent liquids were loaded into (stainless steel) sample vessels in a helium purged glove box with a dew point of <-20° C (~1000 ppm H_2O). Before loading, the liquid solvents were degassed in the purged box by directly bubbling helium through the solvents in their storage containers. The solvents were then dispensed using calibrated pipets. Typical sample volumes were 4 cm^3 or 10 cm^3. The samples were then weighed to confirm the liquid loading. After sealing the sample in the sample vessel in the helium-purged box, the sample vessel was attached to a custom built Sieverts apparatus.[5] Next, the sample vessel was cooled with liquid nitrogen. After cooling, the sample vessel was dynamically evacuated while keeping the sample cold. Then the sample was thawed while sealed allowing any remaining dissolved gas to desorb. After completely warming to room temperature, the procedure was repeated for a total of at least 3x. During warming, the solvent vapor filled the sealed volume up to the saturation vapor pressure. This vapor was fully condensed back into the sample vessel upon subsequent cooling steps. The final evacuation was conducted until the system pressure (measured near the pump) was lower than 5 x 10^{-7} Torr.

This procedure first replaced condensable gases with helium and then degased the helium with the sample frozen at 77 K, minimizing the loss of any solvent. For some samples, nearly 20 freeze-pump-thaw cycles were performed with a measured sample loss of <5% of a 10 cm^3 sample. Thus, this procedure should be applicable to confined liquid/scaffold composites containing a specific solvent loading.

4.2 Volumetric solubility measurements: Solubility measurements were obtained by gas-uptake (dissolution) at single pressures using the following procedure. After degassing, the sample was sealed in the sample vessel volume under its saturation vapor pressure. Hydrogen was introduced into a calibrated volume and the initial moles of hydrogen determined after

equilibration at the room temperature. This known amount of hydrogen was then expanded into the sample volume where it dissolved in the solvent. Expansion of the solvent vapor pressure back into the calibrated volume is considered below. During expansion and dissolution, the pressure was recorded at 30 s intervals. As is well known, the dissolution process can be very slow for static liquids, which is why (as described above) most techniques use stirring. To facilitate equilibration we used ultrasonic agitation. The sample fixtures for these measurements were modified to include a thin extension tube, 5 inches long but only 1/16 inch OD. These extensions gave some flexibility to the sample vessel to allow coupling to the ultrasonic energy. The 5 inch length extension also allowed the sample vessel to be dipped into the water bath of a standard laboratory ultrasonic cleaner. The measurement is illustrated in Figure 3, which shows

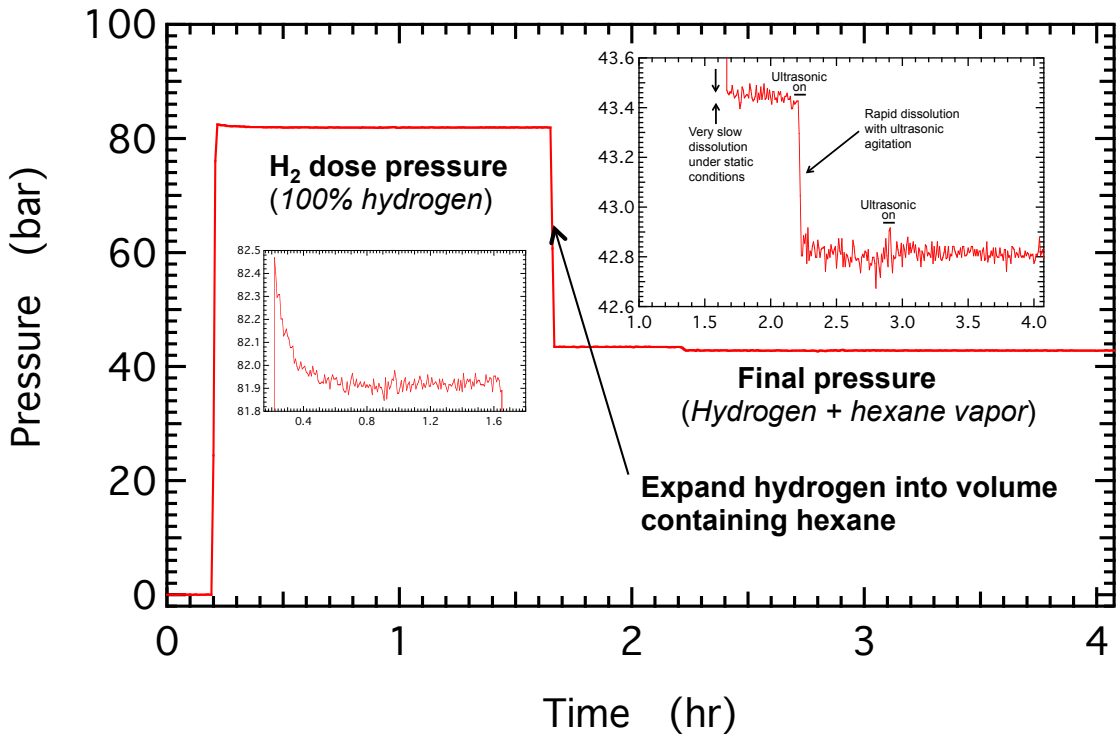

Figure 3. Hydrogen solubility using volumetric measurements in a Sieverts apparatus. System pressure versus time is shown. At 0.2 hr, hydrogen is introduced into a calibrated volume up to a pressure of ~82 bar. Thermal equilibration following pressurization takes ~ 0.5 hr as indicated by the slight decrease in pressure shown in the inset (left). After expanding the equilibrated hydrogen into the sample volume containing ~10 cm^3 of hexane, the pressure decreases to ~43 bar. Under static conditions, from 1.7 hr to 2.2 hr, hydrogen uptake (dissolution) is very slow as shown in the inset (right). During 5 min with ultrasonic agitation, indicated by the line segment under the "Ultrasonic on" label, rapid dissolution occurs. A second ultrasonic treatment at 2.9 hr has no effect indicating that dissolution had reached equilibrium. The final pressure is the sum of the hydrogen pressure and the hexane vapor pressure.

the system pressure versus time. In this example, after thermal equilibration, hydrogen is expanded into the sample volume at ~1.7 hr. Over the next 0.5 hr, hydrogen dissolution occurs very slowly as indicated by the slow decrease in pressure. At ~2.2 hr the ultrasonic cleaner was turned on for 5 min, as shown in the figure by the short line segment under the "Ultrasonic on" label. During this interval a rapid decrease in the pressure occurred indicating rapid dissolution

of hydrogen. The ultrasonic treatment was only used for 5 min intervals because of heating of the water bath. At ~2.9 hr the treatment was repeated but, this time, no noticeable change occurred indicating that the system was at equilibrium. We experimented with different ultrasonic treatments and it seems that dissolution was always close to equilibrium after a single treatment lasting about 3 min. We standardized the procedure to two 5 min treatments at least ½ hr apart. After equilibration, the final system pressure was recorded and used to determine the final moles of hydrogen in the gas phase. The difference between the initial and final moles of hydrogen in the gas phase was used to determine the solubility. Accounting for the vapor pressure of the solvent is discussed below. Finally, due to the low solubility of hydrogen in bulk liquids, <0.2 wt% at pressures <100 bar, a background correction was applied. The background was measured using a sample "blank," a machined cylinder of aluminum with a geometrically determined volume. Background points were measured over a range of pressures using blanks with volumes close to actual sample volumes. These steps constituted a single point solubility measurement. After each measurement, the sample was degassed 3x and the measurement repeated at a different pressure. This procedure achieves equilibrium solubility without macroscopic stirring by using ultrasonic agitation coupled through a water bath and the stainless steel sample vessel to a bulk liquid sample. Sufficient coupling is also expected to occur to confined liquids contained in particulate scaffolds.

4.3 Consideration of solvent vapor pressure: For volumetric measurements of gas solubility in volatile solvents, the solvent vapor pressure must be taken into account. We began by simply monitoring the equilibrium vapor pressure of thoroughly degassed solvent over times at different ambient temperatures. We note that except for the sample vessels, which may be actively heated and cooled, the other volumes of our Sieverts apparatus are at ambient laboratory temperature. The result for hexane is shown in Figure 4. By monitoring the pressure on different days we

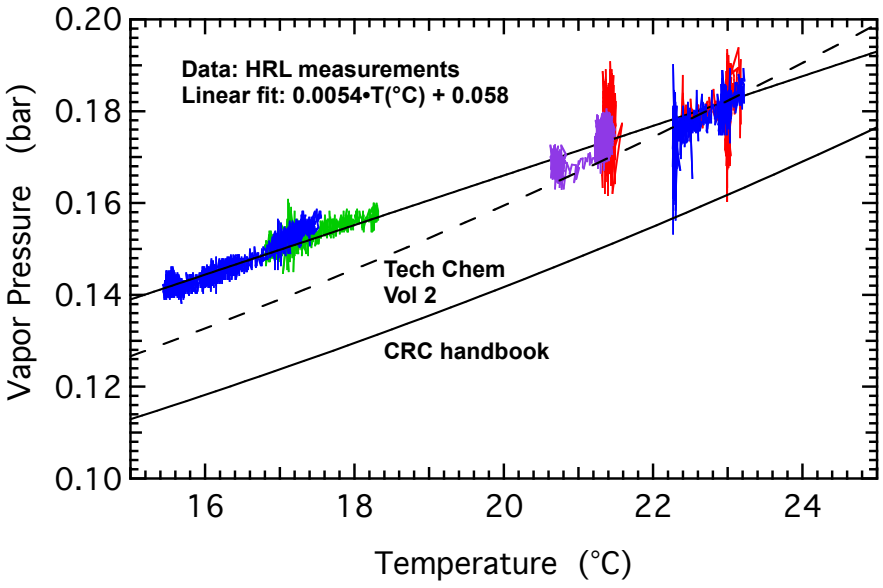

Figure 4. Vapor pressure of hexane versus temperature. The data show the system pressure containing only pure hexane vapor as a function of laboratory ambient temperature. The different data groupings were obtained by monitoring the hexane pressure at different times on different days. This data was fit with a linear dependence given by the equation shown. The vapor pressure from two reference sources is also shown.

obtained equilibrium pressure measurements over a range of ambient temperatures from 16° C to 23° C. The fit shown is a straight line. Although formally the vapor pressure depends exponentially on temperature, a linear dependence is sufficient over the small temperature range encountered in our laboratory. Our measurements are also within ~10% of handbook values, given by the dashed line. Using these data, the final pressure (as described above) can be corrected for the solvent vapor pressure.

At this point we encountered an unresolved issue. Although the data in Figure 4 are accurate, it appears that the equilibration time for the solvent vapor is extremely long (e.g., 80 hr) in the presence of even a low (e.g., 1 bar) pressure of hydrogen. We did not fully resolve the cause of this effect but it may originate from the thin extension tube (described above) used to be able to agitate the samples using the ultrasonic cleaner. The rate of gas phase diffusion within the extension tube may be very slow. The effect is illustrated in Figure 5, which shows the system pressure over ~6 days. At ~3 hr, hydrogen is expanded from a reservoir volume into the sample vessel. The pressure immediately after expansion is 1.09 bar. Over the next ~80 hr the pressure rises to 1.24 bar. This increase corresponds to the evaporation of the solvent (hexane) to fill the reservoir volume with solvent vapor. At lower pressures the equilibration time is shorter, e.g., ~10 hr at 0.2 bar, while with no hydrogen present (only solvent vapor), equilibrium is established in minutes. These long equilibration times prevent simply correcting the final system pressure using the equilibrium solvent vapor pressure. Thus, two limiting conditions were assumed. Specifically, solubility calculations were performed twice, first assuming that the solvent vapor pressure was zero and second assuming the equilibrium pressure. An average of these two values was used with the individual values used as error limits. This procedure is discussed further below.

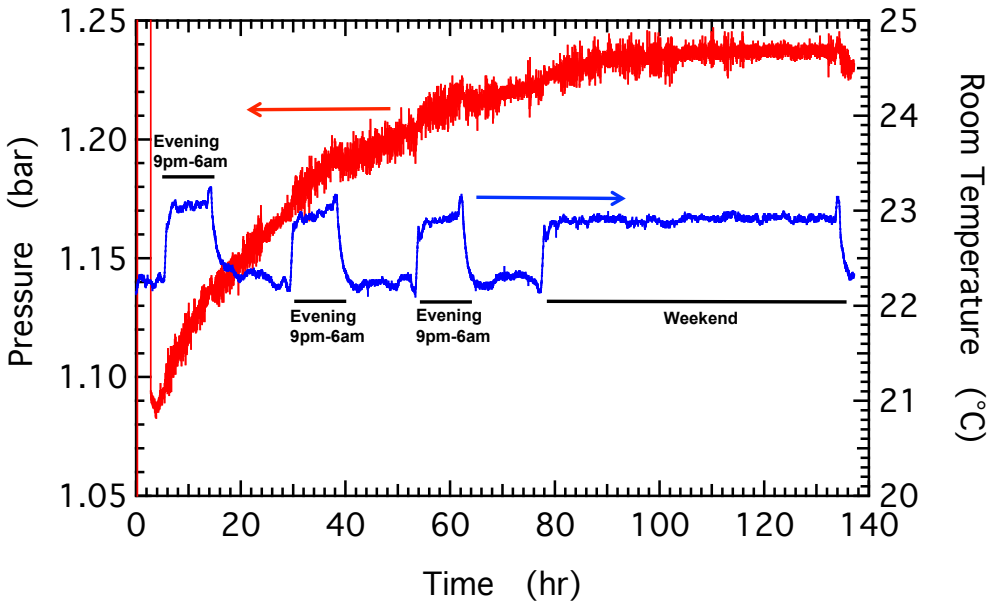

Figure 5. Equilibration of solvent vapor pressure. After expanding hydrogen from a reservoir into the sample volume (at ~3 hr), the system pressure is monitored while hexane evaporated and the vapor diffused to fill the reservoir volume. Equilibration takes ~80 hr. The ambient temperature is also shown. During working hours, the temperature is very stable at ~22.3 ±0.2° C while it rises to ~23° C during the evenings and weekends.

4.4 Solubility of hydrogen in (bulk) n-hexane: Using the procedures described above, the solubility of hydrogen in bulk n-hexane was measured using two custom built Sieverts apparatus designated S1 and S3. The results are shown in Figure 6 together with published state-of-the-art data. For Sieverts apparatus S1, a 10 cm^3 sample was used while for Sieverts S3 the sample size was 4 cm^3. As described above, each point was measured separately and the error bars reflect the uncertainty in the solvent vapor pressure. The positive error direction gives the solubility assuming that the solvent vapor pressure was at its equilibrium value, while the negative error direction originates from assuming that the solvent vapor pressure was zero. The uncertainties are rather large, ~30% at 30 bar. This level of uncertainty prevented measurements below 10 bar. In addition, due to the low capacities (<0.1 wt%) a background correction based on measurements on blank samples was applied. The corrections were also rather large, ranging (depending on pressure) from 20% to 35% and 30% to 50% for Sieverts S1 and S3, respectively. Nevertheless, given these uncertainties and corrections, the average values appear, as expected, linearly dependent on pressure. In addition the slopes of the linear fits are nearly identical for both apparatus, which used sample sizes differing by 2.5x. Finally, compared to published state-of-the-art values, the measured solubilities are similar, ~15% lower.

These data demonstrate that Sieverts apparatus techniques can be used to reproducibly and accurately measure the solubility (storage capacity) of hydrogen in (bulk) solvent liquids in a fashion amenable to similar measurements on nano-confined liquids.

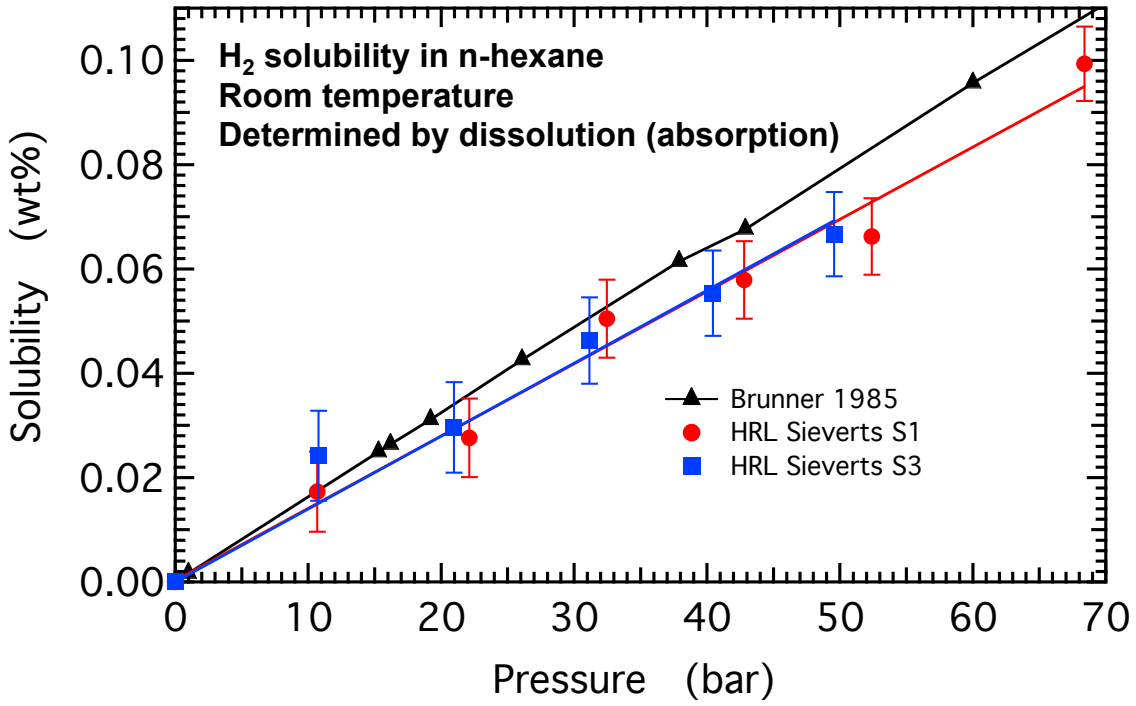

Figure 6. Hydrogen solubility in n-hexane. Using the procedures described in the text, the solubility of hydrogen was measured using two HRL Sieverts apparatus; S1: solid circles, 10 cm^3 sample and S3: solid squares, 4 cm^3 sample. Published state-of-the-art values are from Ref. 1 at 298.15 K. The Henry's law constants, proportional to the slope of the linear fits, are nearly equal for the two apparatus but ~15% lower than the published value.

4.5 Fabrication of nano-confined liquid/nano-porous scaffold composites: To study and verify the solubility enhancements of nano-confined liquids, it was necessary to prepare composites consisting of solvent liquids incorporated within the pore volume of nano-porous scaffold supports. These composites had to have adjustable solvent loadings while being as homogeneous as possible. To prepare such composites the following procedure was developed. First, a desired amount of the empty scaffold was load into a weighed sample vessel. The scaffold in the sample vessel was then degassed by heating to 250 °C under dynamic vacuum for 10 hr. This step removed adsorbed water, typically 1 to 5 wt%. The sealed sample vessel was then opened in a helium-purged glove box and weighed to determine the mass of the degassed scaffold. Next, the liquid solvent was added and the vessel weighed again to determine the solvent mass and, using the known solvent density and the pore volume of the scaffold, the scaffold volumetric loading (vol% = cm^3-solvent/cm^3-scaffold pore volume • 100%). Initial loadings were chosen to be ~85 to 90 vol%. For example, the specific pore volume of MCM-41 is 1.04 cm^3/g (see scaffold characterization below) and the density of n-hexane is 0.659 g/cm^3. Thus, for a 5 g sample of MCM-41, there is 5.2 cm^3 of pore volume. A mass of n-hexane of 2.91 g would occupy 4.42 cm^3 (= 2.91 g/0.659 g/cm^3) or 85 vol%. To best ensure that the hexane was homogeneously confined within the pore volume of the scaffold and not simply between the particles of scaffold or at the bottom of the sample vessel, the composite was uniformly heated (in a sealed sample vessel) to 60 °C overnight and then cooled slowly over ~2 hr. At 60 °C, hexane has a vapor pressure of nearly 1 bar and so should displace the helium and distribute into the pores. This is thermodynamically the most stable configuration. After fabrication and homogenization, the composite (under helium) was evacuated using three freeze/pump/thaw cycles and the hydrogen uptake (solubility) measured as described above for bulk liquids. To achieve lower volumetric loadings, known amounts of solvent where evaporated from the composites using the solvent vapor pressure and the calibrated volumes of the Sieverts apparatus. After reducing the solvent loading by evaporation, the composite was homogenized again using the heat treatment at 60 °C.

4.6 Hydrogen solubility in n-hexane/MCM-41 composites: Using the procedures given above, initial measurements of the solubility of hexane confined within the pore volume of MCM-41 were performed. The hexane/MCM-41 composite was chosen because two publications from the CNRS group reported consistent results for this system, a 16x and 15.9x solubility enhancements, respectively.[2, 6] In addition, MCM-41 is a well characterized commercially available mesoporous silica with 1-dimensional hexagonal cross section pores, Figure 7. The CNRS group prepared their MCM-41 in-house; we purchased MCM-41 from ACS Material, LLC (7). The CNRS material was reported to have a BET specific surface area of 1065 m^2/g, a mesopore volume of 1.09 cm^3/g, and a mean pore size of 3.4 nm.[2] Similar values: surface area of 930 m^2/g, mesopore volume of 1.22 cm^3/g, and mean pore size of 3.7 nm were obtained from nitrogen adsorption analysis of the ACS Material sample. A schematic visualization of the hexane, the MCM-41 porous scaffold, and the approximate size ratio of the hexane to the pore is shown in Figure 7.

The hydrogen solubility results for hydrogen dissolution in hexane confined within MCM-41 at hexane loadings of 52 vol%, 76 vol%, and 84 vol% are shown in Figure 8. Beginning with a composite in which 84% of the pore volume of the MCM-41 was filled with hexane, three independent single point hydrogen solubility measurements were obtained at ~40 bar. Within

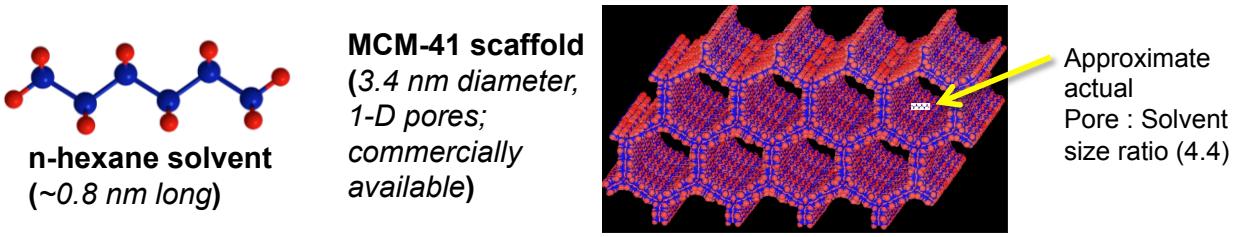

Figure 7. Schematics of hexane, MCM-41 scaffold, and pore:solvent size ratio.

the uncertainties given by the error bars, all three measurements are similar to those measured for bulk hexane. The lowest solubility point was measured first. The second and third measurements are nearly identical and slightly higher than the bulk. This may simply be statistical variation, although it might indicate some conditioning of the sample on the first cycle and a slightly higher than bulk solubility. *Note: to compare with the bulk liquid, these measurements ignore the presence of the scaffold. The effect of adsorption on the scaffold is discussed below.* After three measurements at 40 bar a forth measurement was made a 10 bar. As shown, the solubility at 10 bar and the dependence on pressure are also similar to bulk hexane.

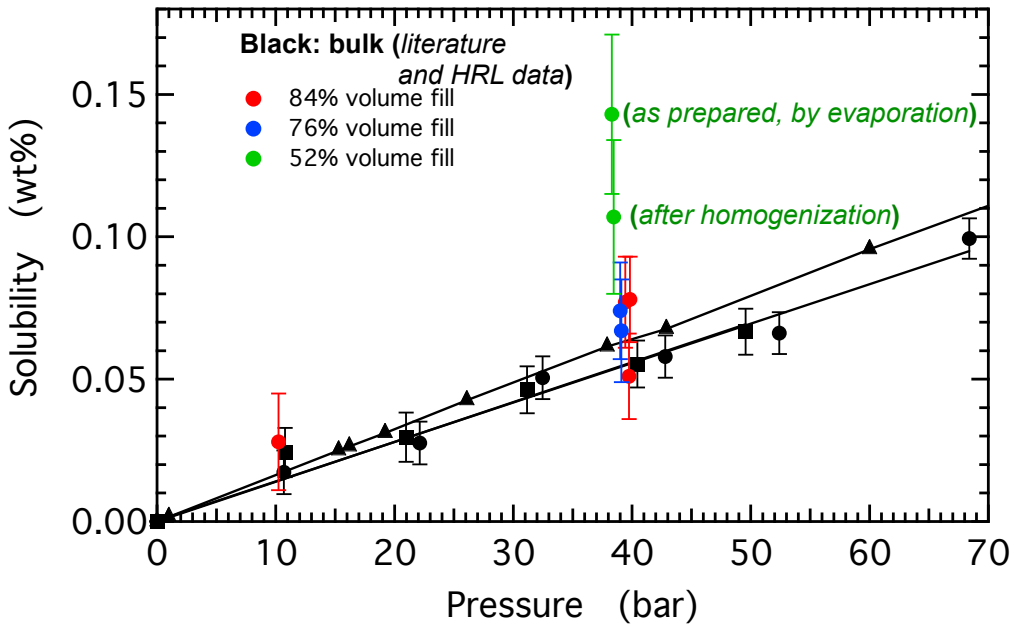

Figure 8. Hydrogen solubility in n-hexane/MCM-41 composites. Black symbols show hydrogen solubility in bulk hexane from the (solid triangles) and from HRL measurements (squares and circles) reproduced from Figure 6. Solubility for hydrogen in hexane/MCM-41 composites is shown for 84 vol% (red), 76 vol% (blue) and 52 vol% (green) hexane loadings. Data for 52 vol% loading are shown before (as prepared by evaporation) and after homogenization. The solubility is calculated based on the mass of hexane only.

Next, a portion of the hexane was removed by evaporation down to 76 vol% loading and the sample homogenized (as described above). Duplicate measurements at 40 bar were nearly identical to the measurements with 84 vol% fill. The solubilities are slightly higher than for the bulk but, again, no significant difference observed. Additional hexane was then evaporated, down to 52 vol% fill. This time the solubility was measured before homogenization. The result shows clear enhancement relative to the bulk, slightly greater than 2x, although the uncertainty is larger due to the decreased mass of hexane. However, after homogenizing the sample, the solubility decreases. This decrease likely indicates that the evaporation of hexane occurred predominately from the surface of the sample, which exposed some empty MCM-41 scaffold. After homogenization, which at least partially filled all of the pores, the solubility was lowered. The solubility after homogenization at 52 vol% fill is still greater than the bulk solubility, by ~2x, but as noted above, these measurements do not account for the effect of the scaffold.

Overall, these initial measurements show at most an ~2x increase in solubility for nano-confined hexane relative to bulk hexane. This value clearly does not agree with published measurements, which report a 16x enhancement at 1 to 4 bar and a volume loading of 60 vol%, for as best as we can tell, an identical solvent/scaffold composite.

4.7 Effect of scaffold adsorption on the measure of enhanced solubility: The data in Figure 8 and in early references from the CNRS group portray the enhanced solubility relative to the confined liquid only. For application to hydrogen storage, the measure of enhanced solubility must include the effect of adsorption on the scaffold. The scaffolds used for nano-confinement of the solvent liquids are nanoporous with moderate to (ideally) high pore volumes and, therefore, high surface areas. Thus significant hydrogen uptake is possible from the scaffold itself, especially if the scaffold is not completely filled with the solvent, ie vol% filling < 100%. Indeed, for any nano-confined solvent/nanoporous scaffold composite to be advantageous for hydrogen storage over simply the empty scaffold, the enhanced solubility in the confined solvent must exceed the adsorption on the empty scaffold. One straightforward measure of this possible advantage is to quantify the enhanced solubility in terms of the amount of hydrogen stored per unit volume of scaffold pore volume, in other words, the pore volume-volumetric hydrogen density. A convenient unit for this amount is mmol-H_2/cm^3-pore volume. For an empty scaffold, a lower limit of this measure is given by the excess adsorption per unit volume of scaffold pore volume. Using the excess adsorption gives a lower limit because it does not count the gas phase hydrogen that fills the pore volume. For a bulk liquid, this measure is simply the volumetric solubility, mol/L, which equals mmol/cm^3. This measure of the enhanced solubility was used by the CNRS group in a more recent publication.[6] In this work the excess solubility for hydrogen in the hexane/MCM-41 composite (60 vol% loading) was 15.9x relative to the bulk solubility, in agreement with an earlier measurement of 16x.[2] The pore volume-volumetric hydrogen density at ~35 bar was reported to be 2.7 mmol/cm^3, which was 3.1x the density for bulk hexane, 0.17 mmol/cm^3. This enhancement (3.1x) is much smaller than the enhancement relative to bulk hexane (16x) but, nevertheless, it is still an enhancement. We followed the analysis of the CNRS group and determined the pore volume-volumetric density for the data in Figure 8. The results as a function of scaffold loading are shown in Figure 9.

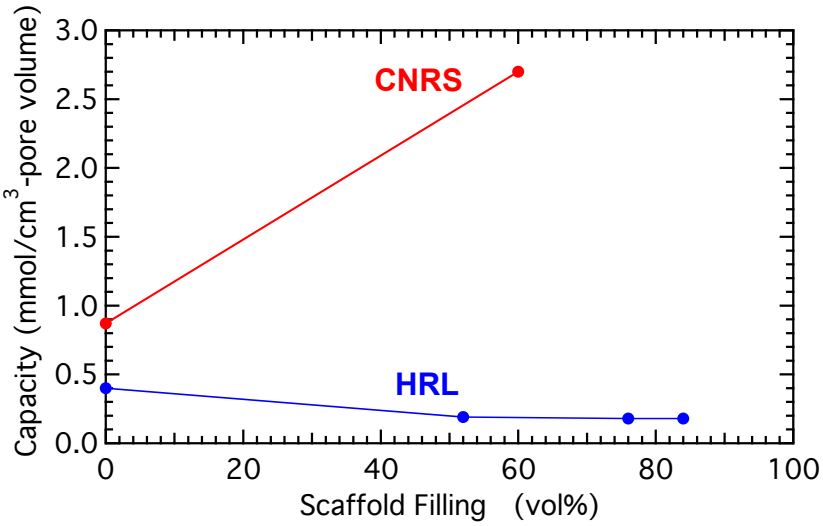

Figure 9. Pore volume-volumetric hydrogen storage in n-hexane/MCM-41 composites. Blue symbols show HRL data at 40 bar. Red symbols show data from Ref. 6 at ~35 bar.

For the empty MCM-41 scaffold the capacities reported by the CNRS group and determined in this project differ by ~2x. However, more importantly, filling the scaffold with hexane to ~60 vol% loading significantly increases the capacity in the CNRS data while the capacity decreases to the capacity for bulk hexane in the HRL data. A tabular summary of the CNRS and the HRL data is shown in Table 1.

Table 1. Comparision of CNRS and HRL data for hydrogen solubility in bulk hexane and nano-confined hexane/nanoporous MCM-41 composites.

	Bulk n-Hexane* ($mmol/cm^3$)	Empty MCM-41* ($mmol/cm^3$)	Composite Hexane/MCM-41* ($mmol/cm^3$)	Capacity wrt bulk hexane	Capacity wrt empty MCM-41
CNRS Chem Phys Lett 2010 JACS 2012	**0.17**	**0.87**	**2.7** (*60 vol%*)	**15.9** x large enhancement	**3.1** x large enhancement
HRL	**0.185**	**0.4 ± 0.1**	*0.19 (52 vol%)* *0.18 (76 vol%)* *0.18 (84 vol%)*	**1.03** x **0.97** x **0.97** x no enhancement	**0.48** x **0.45** x **0.45** x lower

*All measurements at ~35 bar

4.8 Interaction with the CNRS group: We were unable to reconcile the CNRS and HRL data. The CNRS group was contacted with assistance from Dr. Thomas Autrey and coworkers at PNNL. The current project PI, Professor David Farrusseng, cautioned us about the difficulties of working with hexane due to it volatility. As described above, we were well aware of the volatility of hexane and took extensive measures to ensure that the composites were prepared with accurately know loadings, that the loading was uniform, and that little (<5%) loss of hexane occurred during measurement. The original PI, Professor Marc Pera-Titus, was also contacted. He stated that although seemingly simple, performing measurements on liquid nanocomposites

was not straightforward. Unfortunately, additional details were not obtained due to confidentially issues.

To attempt to understand the origin of the differences between the published results and the current HRL results, the CNRS experimental procedure described in Ref. 6 was duplicated as closely as possible. Following the CNRS procedure, ~1 g of MCM-41 was loaded (in air) into a sample vessel. Next 0.49 cm^3 of hexane (an ~50% volume loading) was added and the sample was attached to a Sieverts apparatus. To mimic the reported "gentle evacuation", apparently at room temperature, the sample was evacuated to 0.7 Torr (over ~3 to 4 min). After removing the sample and weighing, we determined that ~55% of the hexane was lost by this evacuation procedure. At this point we are uncertain how the CNRS samples were treated without significant loss of hexane. Note: the HRL evacuation procedure involves freeze/pump/thaw cycles which was verified to result in <5% solvent loss even after 20 cycles.

5. Accomplishment — Optimization of liquid/scaffold composite for enhanced hydrogen solubility: Because the publish results for the hexane/MCM-41 composite could not be verified, a variety of other solvent/scaffold combinations were examined in order to maximize the hydrogen capacity.

The liquid solvents examined are shown schematically in Figure 10, they include:

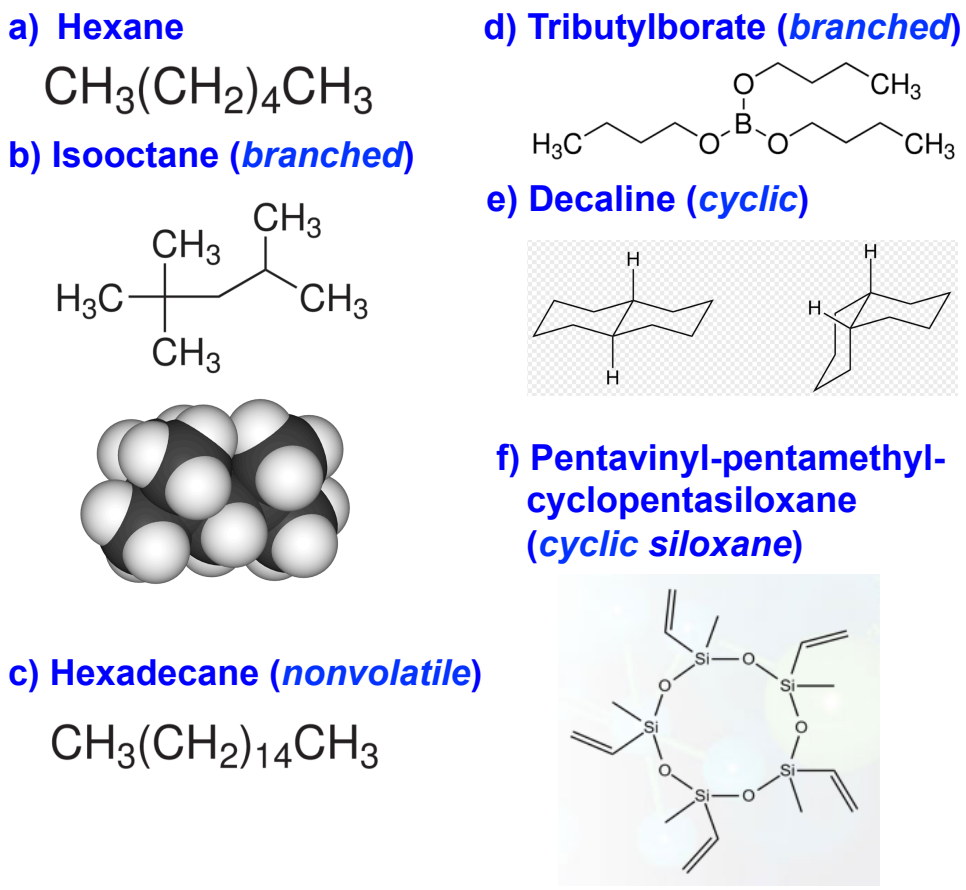

Figure 10. Liquid solvents examined.

• Hexadecane ($C_{16}H_{34}$): This solvent was chosen because it is similar to hexane (C_6H_{14}) in that both are fully saturated linear alkanes. Hexadecane is much less volatile than hexane with a boiling point of 287 °C compared to ~65 °C for hexane. This makes composites with hexadecane much easier to prepare and, in addition, no vapor pressure correction is needed because the vapor pressure is negligible at room temperature. Hexadecane was obtained from Aldrich, product H6703.
• Decaline ($C_{10}H_{18}$): This solvent, suggested by Professor David Dixon, is a cyclic saturated alkane with two isomers, *cis* and *trans* as shown in Figure 10. A mixture of the two isomers was used. The boiling point is ~190 °C, thus no vapor pressure correction was needed. Decaline was obtained from Aldrich, product 294772.
• Tributylborate: This solvent is essentially a branched saturated alkane with three linear butyl groups anchored around a BO_3 core. The branched geometry of this solvent may make its packing within pores inefficient. Tributylborate was obtained from Aldrich, product 90795.
• Pentavinyl-pentamethyl-cyclopentasiloxane: This high molecular weight (MW = 430.82 g/mol) cyclic siloxane is still a liquid indicating weak intermolecular interactions. Pentavinyl-pentamethyl-cyclopentasiloxane was obtained from Gelest, product SIP6719.7.

In addition to the mesoporous silica MCM-41 described above, the scaffolds examined include:
• PICA activated carbon: This scaffold is a coconut-based activated carbon with two-dimensional slit pores predominately <2 nm in width. It consists of irregular granules ~ 2 mm to 5 mm in size. This granular consistency facilitated preparation of the composite. In contrast, the MCM-41 was a fine, micrometer sized, powder that was difficult to handle and pack to high densities. This scaffold was obtained, as a sample, from PICA USA, Inc, product G55C-1.
• Zeolite 4A: This scaffold was tested in two forms. The first was in the form of ~ 2 mm diameter beads (8 – 12 mesh). Similar to the activated carbon granules, the beads facilitated preparing the composites and in particular determining the 100 vol% loading level. This level was easily determined for the beads because at lower loadings, the beads appeared dry and a sample (consisting of many beads) flowed easily. In contrast, at loadings as low as ~105 vol%, the beads appeared wet and samples of the beads were sticky and did not flow. However, the beads contain filler in order to bind the zeolite powder. Typical formulations specify binder levels of ~20%, however, the actual level in the beads used was not known. The zeolite 4A beads were obtained from Aldrich, product 208604. Although more difficult to handle, a fine powder form (<5 micrometers) of zeolite 4A was also tested. It was obtained from Aldrich, product 233668.
• Chabazite zeolite: This scaffold is a natural (mined) form of zeolite with a structure similar to zeolite 4A. It was obtained as a sample from GSA Resources, Inc, product Carbasorb ZS500A, in the form of irregular granules ~ 5 mm in size (8).
• Carbon aerogel: This scaffold was a resorcinol-formaldehyde aerogel with a 4.8 nm mode pore size. It was obtained from Marketech (9) in the form of large, 1 cm to > 5 cm, irregular monolithic chunks. These chunks were broken and ground into ~ 1 mm size shards and sieved to be >230 mesh (>0.06 mm).

5.1 Enhanced solubility in hexane/PICA activated carbon composites: Hexane/PICA activated carbon composites were examined over both a range of pressures and a range of solvent loadings. The data were also analyzed using a preexisting system volume calibration and after a

careful recalibration. This recalculation illustrated the sensitivity of these enhanced solubility measurements to the system volumes. The results are shown in Figure 11.

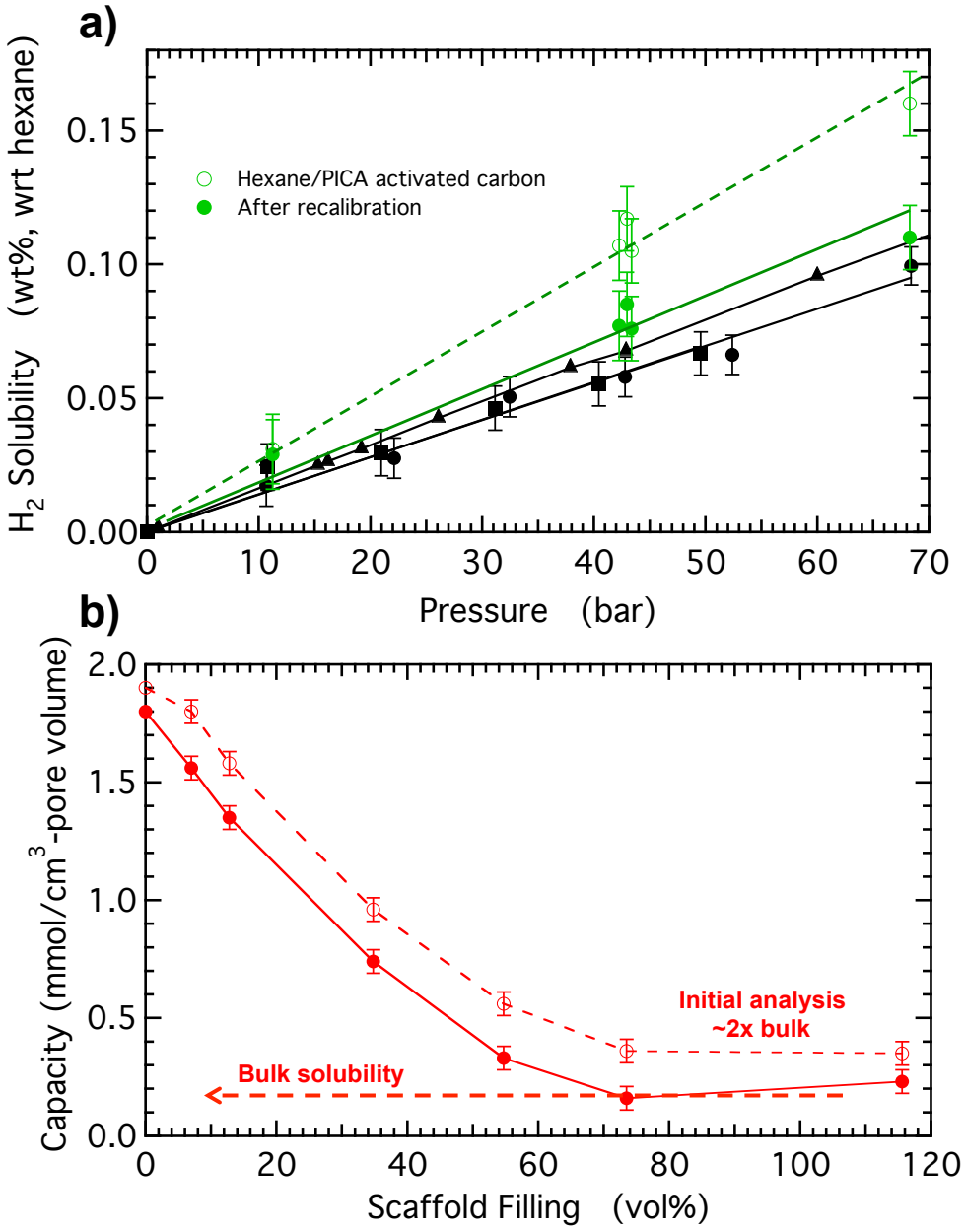

Figure 11. Enhanced solubility of hydrogen in hexane/PICA activated carbon composites. a) Gravimetric hydrogen solubility relative to hexane only versus hydrogen pressure for bulk hexane (black triangles from Ref. 1, black circles and squares with error bars from HRL measurements on two different Sieverts apparatus) and for composites with a hexane volume loading of 119 vol% using preexisting system volume calibrations (green open circles and dashed line) and carefully recalibrated volumes (green filled circles and solid line). b) Pore volume-volumetric hydrogen capacity at ~ 40 bar versus scaffold filling using preexisting volume calibrations (red open circles, labeled initial analysis) and carefully recalibrated volumes (red filled circles). The volumetric bulk solubility is indicated. For both gravimetric and volumetric measures, the enhancement of ~2x relative to the bulk is seen to be an artifact of slight calibration errors in the system volumes.

Using a preexisting system volume calibration performed in 2004, hexane/PICA activated carbon composites appeared to show a solubility enhancement for hydrogen of ~2x. The enhancement relative to the gravimetric solubility of bulk hexane was clearly seen over a range of hydrogen pressures (Figure 11a). The pore volume-volumetric hydrogen capacity for the composite as a whole decreased with hexane loading indicating that this composite would not be useful for hydrogen storage. The capacity decreased up to a loading of ~ 70 vol% and was then independent of loading up to at least ~120 vol%. However, unlike the hexane/MCM-41 composite described above, the decreased capacity reached a minimum at a value 2x the bulk hexane. These data could represent an actual enhanced solubility.

5.2 Effect of system volume calibrations on enhanced solubility measurements: The initial measurements for the hexane/PICA activated carbon composite clearly showed a solubility enhancement of ~2x. In the course of these measurements, the empty scaffold skeletal volume (V_s) is determined from the calibrated system volumes using helium. This volume is needed to determine the free gas volume of the sample vessel when the sample vessel contains a sample. From this volume the empty scaffold skeletal density can be determine using the measured scaffold mass. After a thorough vacuum bake-out to remove any adsorbed water, the measured density was 1.95 ± 0.02 g/cm^3, where the uncertainty represents the standard deviation of approximately 10 measurements. This value is low (by ~8%) compared to many porous carbon materials that are known to have typical densities of ~2.1 g/cm^3. This apparently low density is important because if a typical density of 2.1 g/cm^3 was assumed and then the V_s calculated and used to determine the free gas volume of the sample vessel, no solubility enhancement was seen.

To check for errors in the calibrated system volumes that might lead to an erroneously low scaffold density, the system volumes were carefully recalibrated. The recalibrated system volumes where very close to, within ±0.6% of, the previously measured volumes (measured in 2004). However, these small differences did indeed account for an 8% too small sample density. To illustrate the sensitivity of these measurements to the system calibrations an example is given. A typical sample volume (V_s) calculation uses an expression such as:

$$V_s = V_{1sv4} - 0.6665 \bullet (V_2 + V_3)$$

where V_{1sv4} is the calibrated volume for sample vessel SV-4 (when empty) and ($V_2 + V_3$) is the calibrated reservoir volume. The factor 0.6665 comes from the ratio of (one run of) the measured pressures before and after expansion. The original V_{1sv4} was 42.2426 cm^3 while the recalibrated V_{1sv4} was 41.9824 cm^3, only ~0.6% smaller. For ($V_2 + V_3$), the original measurement was 56.6818 cm^3, while the recalibration gave 56.8490 cm^3, only ~0.3% larger. Thus, calculation of V_s using the original and recalibrated system volumes gave:

Original 2004 calibration: $V_s = 42.2426 - 0.6665 \bullet (56.6818) = 4.4642$ cm^3

2013 recalibration: $V_s = 41.9824 - 0.6665 \bullet (56.8490) = 4.0925$ cm^3

The sample volume based on the original 2004 calibration is 9% larger, which accounts for the low sample density. This sensitivity, -0.6% and +0.3% variation in system volumes leading to a 9% difference in sample volume, arises because the computation involves the difference of two similar numbers to give a number ~10x smaller. This example demonstrates the need for high quality system calibration especially when measuring small hydrogen storage capacities.

Using the recalibrated system volumes the measured density of the PICA activated carbon scaffold was determined to be 2.13 g/cm^3. This value is now in the expected range for porous

carbon materials. Unfortunately, as described above, using this density gives no enhancement for the solubility of hydrogen in hexane/PICA activated carbon as shown in Figure 11 for both the gravimetric and volumetric solubility measures. The apparent 2x enhancement was an artifact from slight errors in the system volumes.

To finalize evaluation of the hexane/PICA composite, a separate Sieverts apparatus was used. With this system, the PICA activated carbon density was measured to be 2.10 g/cm^3 in agreement with the recalibrated density discussed above. In addition, essentially no solubility enhancement was measured, <1.2x.

5.3 Enhanced solubility in hexadecane/MCM-41 composites: Composites using hexadecane instead of hexane were examined to remove some of the uncertainties associated with the volatility of hexane. Hexadecane is a much longer molecule than hexane. However, it can access similar size pores because its critical diameter for diffusion, 0.49 nm (7), is determined by the cross section of the linear carbon backbone, not the length. Thus, hexane also has a critical diameter of 0.49 nm.(7) For a composite with a hexadecane loading of 85 vol%, the pore volume-volumetric capacity at 40 bar was 0.17 mmol/cm^3. This can be compared with a bulk solubility of 0.15 mmol/cm^3. Thus essentially no enhancement (at most 1.1x) was seen for this composite.

5.4 Enhanced solubility in hexadecane/zeolite 4A composites: Initial hexadecane/zeolite 4A composites were based on zeolite 4A in the form of beads. Work began with this form because of the ease of working with the beads, in contrast to the difficulty of working with fine powders. The pore volume-volumetric hydrogen capacity with difference hexadecane loadings is shown in Figure 12. Surprisingly, the capacity is independent of loading; the empty scaffold capacity is retained as hexadecane is added up to ~115 vol%. No increase above the empty scaffold capacity is seen.

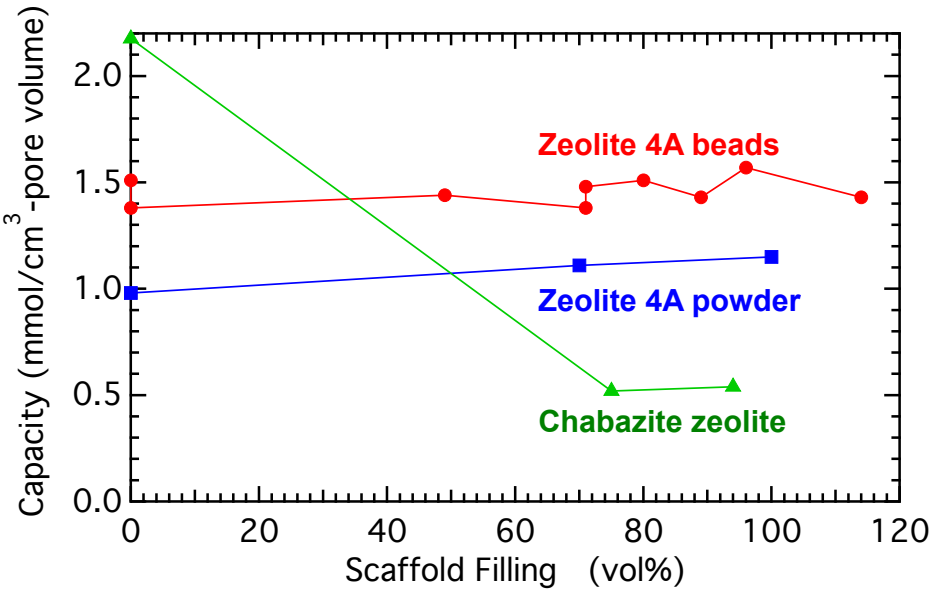

Figure 12. Pore volume-volumetric hydrogen capacity of hexadecane/zeolite-based composites. Capacities are shown at 40 bar hydrogen versus hexadecane loading (vol%) for zeolite 4A beads, zeolite 4A powder, and Chabazite zeolite. Multiple samples of the zeolite 4A beads were tested.

A straightforward explanation for this behavior is that the hexadecane simply did not infiltrate the pores leaving the adsorptive capacity for hydrogen unaffected by the added solvent. To explore this possibility, simple bench-top solvent-uptake experiments were performed. As mentioned above, the 100 vol% loading level of the beads was easily determined because as solvent was added and mixed for several minutes (~4 g samples were used for these rests), the sample became dry and flowed easily up to a relatively specific loading where the beads abruptly appeared wet and became sticky and no longer flowed. The 100 vol% loading was determined by weighing the added solvent and expressed as the volume of solvent per unit mass of scaffold (cm^3-solvent/g-scaffold). The solvent volume was determined from the mass of the solvent using the tabulated bulk solvent density. For hexadecane, 100 vol% loading occurred at 0.26 cm^3/g, *i.e.*, at 0.25 cm^3/g the sample was dry and flowed easily; at 0.27 cm^3/g the sample was wet and sticky. This value was compared to the 100 vol% loading for water and methanol. These molecules are considerably smaller than hexadecane with critical diameters of 0.32 nm (H_2O) and 0.44 nm (CH_3OH).(10) The results are shown in Table 2. Water and methanol are expected to fill the zeolite 4A pore volume and, as expected, the 100 vol% loading for both solvents are nearly identical, 0.32 cm^3/g. The 100 vol% loading for the hexadecane (0.26 cm^3/g) is clearly lower than for water and methanol but it is lower by only ~20%. Thus, it seems that hexadecane is filling a large portion of the zeolite 4A pore volume. How the volumetric hydrogen capacity of the hexadecane/zeolite 4A remains constant at the empty zeolite 4A level is not known.

Table 2. Solvent characteristics and loading of zeolite 4A beads.

Solvent	Critical diameter (nm) Reference 6	Solvent density (g/cm^3)	Dry appearance maximum loading (cm^3-solvent/g-zeolite)	Wet appearance minimum loading (cm^3-solvent/g-zeolite)
Water	0.32	1.0	0.31	0.32
Methanol	0.44	0.792	0.32	0.33
Hexadecane	0.49	0.773	0.25	0.27

Although easy to work with, the zeolite beads contain a binder that could be affecting the results. To check for effects due to the binder, composites were prepared from a pure zeolite 4A powder. The results are shown in Figure 12. The capacity of the empty scaffold is lower for the powder compared with the beads. This is unexpected considering that the added binder in the beads should be nonporous. Nevertheless, the capacity of the zeolite 4A powder is also unchanged with solvent loading.

5.5 Enhanced solubility in hexadecane/Chabazite zeolite composites: To compare with the zeolite 4A-based composites, natural granular Chabazite was used as a scaffold. The irregular millimeter size granules of the Chabazite did not flow like the beads of zeolite 4A. However, the granules were large enough to measure solvent uptake on individual granules. Solvent 100 vol% filling levels for water, methanol, and hexadecane were measured to be 0.47 cm^3/g, 0.48 cm^3/g, and 0.46 cm^3/g, respectively. These similar values indicate that hexadecane is likely filling most of the pore volume of the zeolite. The capacities of hexadecane/Chabazite composites are shown in Figure 12. For Chabazite, the capacity decreases considerably from the empty scaffold but

levels out at a capacity much higher than the bulk solubility. For hexadecane loadings >~80 vol%, the capacity is ~0.55 mmol-H_2/cm^3, which is 4x the bulk solubility.

5.6 Enhanced solubility in solvent/carbon aerogel composites: The MCM-41 and zeolite scaffolds contain pores with essentially single sizes. Carbon aerogel was examined as a scaffold with 3-dimensionally confined pores with a distribution of pore sizes in mesopore range. The specific aerogel studied had a mode (most probable) pore size of 4.8 nm with a distribution from <2 nm to ~ 12 nm. The capacities of different solvent/carbon aerogel composites at ~40 bar hydrogen and ~90 vol% solvent loadings are shown in Figure 13. The empty aerogel scaffold has a pore volume-volumetric capacity of 1.7 mmol-H_2/cm^3-pore volume, which corresponds to 0.19 wt% (at 40 bar and room temperature). The capacity decreases for all the composites tested. The most complete characterization was performed for the hexadecane/carbon aerogel composite. For this composite, the decrease becomes independent of solvent loading beyond ~50 vol% with a retained capacity of 0.75 mmol/cm^3. This capacity is only 45% of the empty scaffold capacity but it is still considerable larger than the bulk solvent solubility. If compared just to the bulk solvent solubility of 0.15 mmol/cm^3, the solubility of hydrogen in hexadecane confined in carbon aerogel with ~5 nm pores is 5x greater (note, however, this may not be a proper comparison).

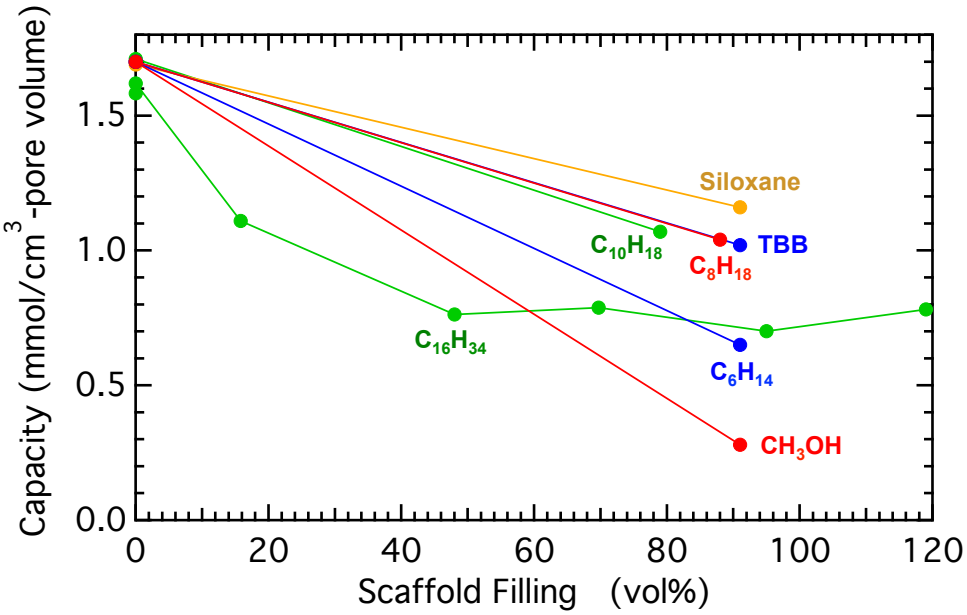

Figure 13. Hydrogen capacities for nano-confined solvent/carbon aerogel composites. Capacities were measured a ~40 bar. Different solvents are as indicated: $C_{16}H_{34}$ = hexadecane, C_6H_{14} = hexane, CH_3OH = methanol, $C_{10}H_{18}$ = decaline, C_8H_{18} = isooctane, Siloxane = pentavinyl-pentamethyl-cyclopentasiloxane, and TBB = tributylborate.

Other composites appear to behave similarly. Hexane/carbon aerogel has a capacity of 0.65 mmol/cm^3 at 92 vol% loading. Hexane and hexadecane might be expected to behave similarly because both molecules are saturated linear alkanes with equal critical diameters. Other non-linear molecules, isooctane and tributylborate, and cyclic molecules, decaline and a cyclic siloxane, have presumably similar dependences with loading but larger retained capacities. The cyclic siloxane, pentavinyl-pentamethyl-cyclopentasiloxane has the largest retain capacity, 1.16 mmol/cm^3, equal to 69% of the empty scaffold capacity. Relative to a bulk solubility of ~0.15

mmol-cm^3, this capacity would represent a ~8x increase in solubility. In contrast, methanol has the smallest capacity, only 16% that of the empty scaffold.

5.7 Mechanism of enhanced solubility: Despite increases relative to the bulk solubility of ~5 to 8x, considering only the bulk liquid might not be a proper comparison. First, the capacities for all of the composites are lower than for the empty aerogel scaffold. Thus, these composites are not useful for hydrogen storage. In addition, the mechanism underlying the retained capacity is not known. One explanation is that the solvents fill some fraction of the larger pores but cannot fit into smaller pores and therefore, the retained hydrogen capacity originates from hydrogen adsorption into the smaller empty pores. This explanation is consistent with the higher capacities for the larger solvent molecules, eg, pentavinyl-pentamethyl-cyclopentasiloxane, and the smallest capacity for the smallest solvent, eg methanol. However, the solvent filling measurements indicate that all of the solvents tested fill >85% of the carbon aerogel pore volume. A summary of the maximum solvent filling measurements and the dependence of the composite hydrogen capacity on the solvent filling is shown in Figure 14 for each solvent tested. The pore volume/surface area relationship for the carbon aerogel scaffold is also shown. This relationship was determined from BJH adsorption analysis of nitrogen isotherms. The pore volume/surface area relationship is depicted as the remaining open (or available) area as a function of the pore volume filled, starting from the largest pores. For example, filling large pores down to a size of 5 nm would fill 55% of the total pore volume, but these pores account for only ~22% of the surface area leaving ~78% of the area open. Similarly, filling pores down to a size of 1.7 nm (the minimum pore size in the analysis) fills 78% of the pore volume but only 50% of the surface area. For pore sizes smaller than 1.7 nm, accounting for pore volumes up to 100%, a linear extrapolation was assumed. The convex form of the relationship indicates that the scaffold surface area is preferentially contained in the smaller pores.

As mentioned above, all of the solvents tested fill 85% of the pore volume. This is not surprising considering that the molecular sizes of the solvents (approximated by the critical diameters (10)) are relatively small, < 1 nm. For example, the critical diameters for hexane and hexadecane (linear alkanes) is 0.49 nm, isooctane (a branched alkane) is 0.56 nm, and tributylborate, estimated using triethylamine, is ~0.84 nm.(10) Comparing the pore volume/open area dependence of the aerogel with the points for the individual solvents shows that the hydrogen capacities of the composites are much higher then the estimated open area. For example, the cyclic siloxane can fill 85% of the pore volume, which from the extrapolation would leave 30% open area; yet the retained hydrogen capacity is 69%, ~ 2x greater. By ratio, the effect is more extreme for smaller solvents. The linear alkanes fill nearly 100% of the pore volume, theoretically leaving no open area; yet the retained capacity is ~30%.

Overall, this comparison indicates that the capacity of the composites cannot be simply explained by hydrogen adsorption into unfilled pores. It seems that at least a portion of the hydrogen capacity of the solvent/carbon aerogel composites must originate from hydrogen contained in solvent filled pores but the mechanism for such adsorption or absorption is unclear. The trend, excluding methanol, suggests that higher capacities might be achieved using larger solvents with lower maximum fillings. If such a trend held, it would seem that maximum solvent fillings of 70% or less would be needed for the composite capacity to exceed 100%, ie the minimum level required to these composites to be useful for hydrogen storage. Based on the pore sizes shown, these solvents would need to very large, 2 nm to 3 nm. Some liquid siloxanes may reach this size. Other possibilities include crown ethers, oligomers or dendrimers.

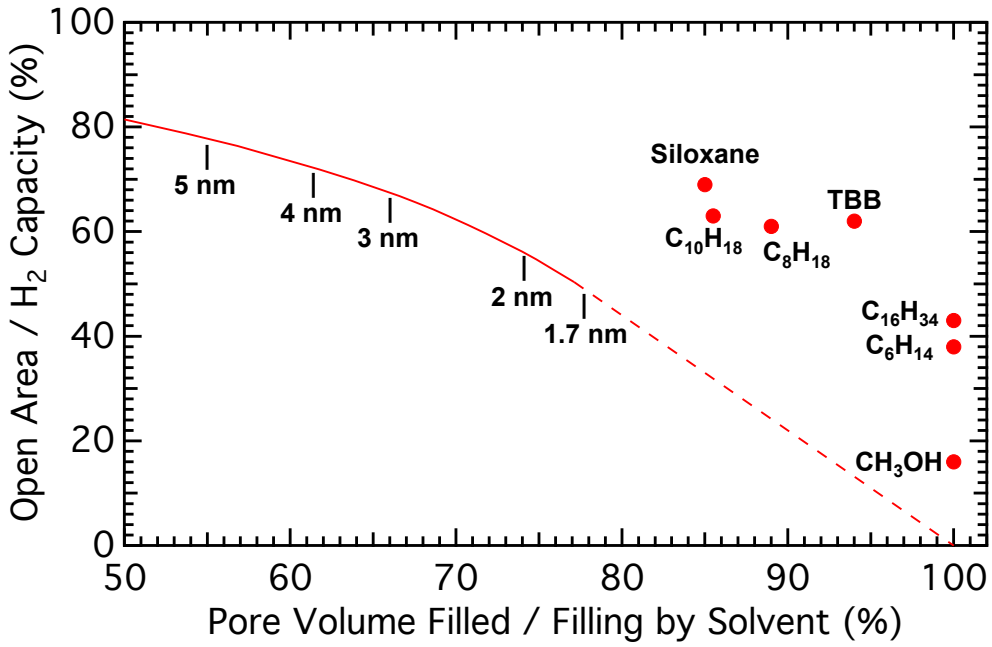

Figure 14. Pore filling/open surface area relationship for carbon aerogel scaffold and solvent filling/retained hydrogen capacity dependence for composites. Solid/dashed line: pore filling/open area relationship; symbols: solvent filling/H_2 capacity dependence. Pore filling/open surface area relationship was calculated from a BJH analysis of the scaffold. The solid line shows the relationship with decreasing pore size (as indicated) down to a pore size of 1.7 nm (the lower limit of the BJH analysis). Beyond 1.7 nm a linear extrapolation (dashed line) is shown. The percent pore volume filled was obtained from the BJH cumulative pore volume by normalization to 100% at 0.56 cm^3/g, which includes addition of 0.06 cm^3/g to account for macropores. The area was obtained from the BJH cumulative area by normalization to 100% using the BET surface area of 670 m^2/g. The open area is given by (100% - percent cumulative area). Solvent filling was determined as described above for hexadecane/zeolite 4A composites but here using ~2 mm to 5 mm chunks of aerogel. The solvent loadings were normalized (to 100%) relative to methanol, which had a maximum loading of 0.56 cm^3/g. Different solvents given by symbols are (as indicated): $C_{16}H_{34}$ = hexadecane, C_6H_{14} = hexane, CH_3OH = methanol, $C_{10}H_{18}$ = decaline, C_8H_{18} = isooctane, Siloxane = pentavinyl-pentamethyl-cyclopentasiloxane, and TBB = tributylborate. Retain H_2 capacity was obtained at 40 bar for ~90 vol% loadings (as shown in Figure 13) normalized to 100% for the empty aerogel.

For the highest capacity composite (pentavinyl-pentamethyl-cyclopentasiloxane/carbon aerogel), the pressure dependence of the capacity (an isotherm) was measured. The results are shown in Figure 15 together with a similar isotherm acquired for an empty carbon aerogel scaffold. The isotherm displays the curvature expected for adsorption, in contrast to the linear Henry's law behavior characteristic of dissolution. The curvature for the composite is more pronounced than it is for the empty scaffold. This suggests that the predominate mechanism for the hydrogen contained within solvent-filled pores might still be adsorption-like where hydrogen is still interacting with adsorption sites such as the aerogel surface area. This mechanism may be distinguished from more dissolution-like behavior in which the hydrogen might be solubilized in the solvent confined within the pore. In addition, the curvature for the composite is more pronounced than it is for the empty scaffold suggesting a higher adsorption energy that, consequently, saturates at a lower pressure. To support these conjectures, direct physical characterization of the hydrogen containing composites would be helpful.

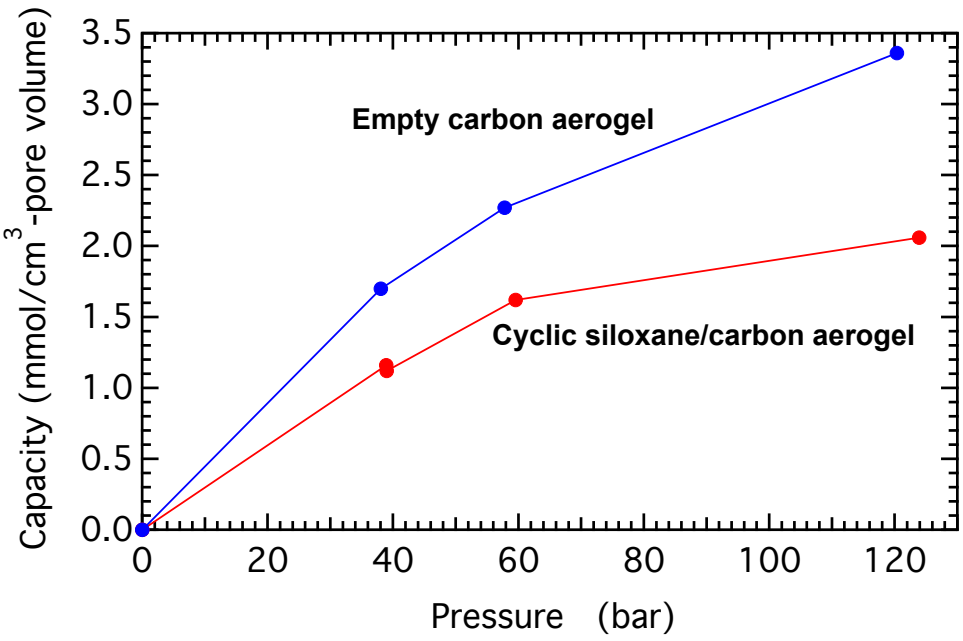

Figure 15. Hydrogen capacity isotherms for nano-confined cyclic siloxane/carbon aerogel scaffold composite and empty carbon aerogel. Capacity is expressed volumetrically relative to the scaffold pore volume. The carbon aerogel had a mode pore size of 4.8 nm, a total pore volume of 0.56 cm^3/g and a surface area of ~660 m^2/g. For reference, the gravimetric capacity at ~120 bar is 0.38 wt%. The cyclic siloxane was pentavinyl-pentamethyl-cyclopentasiloxane, with a loading in the aerogel of 91 vol%. The gravimetric capacity of the composite at ~120 bar is 0.15 wt%. Both isotherms were constructed from individual uptake measurements, ie, the hydrogen was removed between each point. Two points at 40 bar that nearly overlap are shown. One point was the first measurement for this sample while the other point was acquired after subsequent points at 60 and 120 bar. The coincidence of these points indicate that hydrogen uptake in this nano-confined solvent/nanoporous scaffold composite is reversible and can be cycled without degradation for at least 4 cycles.

5.8 Influence of pore structure on enhanced solubility: The hydrogen uptake for composites based on carbon aerogel and PICA activated carbon scaffolds are compared in Figure 16. As described above, the aerogel has 3-dimensionally confined pores with a distribution of pores sizes from < 2 nm to ~12 nm and a most probable (mode) pore size of 4.8 nm. In contrast, the PICA activated carbon is mainly microporous with pore geometries generally thought to be slit-shaped with narrow widths (< 2 nm) in 1-dimension but extended in the other two directions. The pores wall are also likely to be basal planes of graphite and therefore very smooth. The data in Figure 16 indicate that the retained hydrogen capacity of the aerogel-based composites is much higher than for the activated carbon-based composites, which are close to bulk the solubilities. These higher capacities occur despite the aerogel having on average, large pores. Specifically, decaline gives the highest capacities while the capacities for the linear alkanes, hexane and hexadecane, are nearly identical for each scaffold as expected given their equal critical diameters. In addition, based on the more detailed data for hexane/PICA and hexadecane/aerogel, the decrease in capacity with solvent loading is similar for loadings <~ 30 vol%. However, the capacity begins to become independent of the loading at ~50 vol% for the aerogel but not until ~80 vol% for the activated carbon. This difference may originate from the different pore geometries. Although larger, the 3-dimensional confinement in the aerogel may restrict the motion of the solvent within the pores. For the activated carbon, the slit pore shape may allow unrestricted motion in two dimensions. The greater restriction in the aerogel, even

though generally larger, may allow for more of the original (empty scaffold) hydrogen capacity to be retained. This argument may even extend to the MCM-41 scaffold, which also has low composite capacities because it permits unrestricted motion in 1-dimension. Overall, confinement in 3-dimensions may be necessary for significant solubility enhancement.

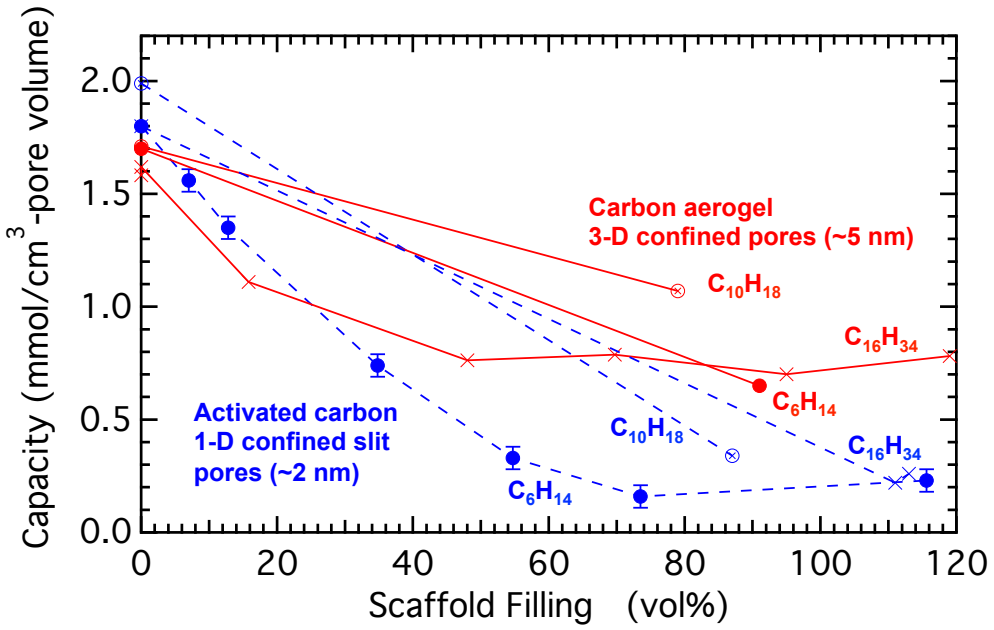

Figure 16. Comparison of retained hydrogen capacities for solvent/carbon aerogel and solvent/activated carbon composites. Carbon aerogel: red, solid lines; PICA activated carbon: blue dashed lines. As labeled, C_6H_{14} = hexane (filled circles), $C_{10}H_{18}$ = decaline (open circles); $C_{16}H_{34}$ = hexadecane (X's).

6. Accomplishment — Molecular level simulations of nano-confined solvents: In addition to enhanced solubility measurements, a second objective of this project was simulation of confined solvents in order to understand the mechanism of gas solubility enhancement and to guide the experimental measurements. To meet this objective a molecular dynamics simulation of fully atomistic molecular hexane interacting, from a bulk reservoir, with a fully atomistic silica nanopore was developed. The simulation was built up in stages by 1) simulating bulk (unconfined) hexane using a 3-dimensional rectangular volume with periodic boundary conditions across all three pairs of opposing walls. Then 2) an idealized confinement condition was studied by fixing the spacing between pairs of opposing walls in one or two dimensions and making the walls perfectly reflective, ie hard-wall confinement. In parallel, 3) a simulation of pure silica was developed containing an approximately cylindrical nano-scale pore and opposing flat silica surfaces, which bounded an empty unconfined volume. This volume was subsequently 4) filled with hexane forming a bulk reservoir and the interaction of hexane from this reservoir with the pore was studied. Finally, 5) hydrogen molecules were introduced into the reservoir with the hexane and their redistribution within the reservoir and pore was briefly studied.

6.1 Details of the simulations: Molecular dynamics (MD) simulations were performed using the large-scale atomic/molecular, massively parallel, molecular dynamics simulator (LAMMPS) developed by Sandia National Laboratories. This code is freely available.(11) The code

performs classical MD simulations using Newton's equation of motion for $>10^9$ particles in solid, liquid, or gaseous states interacting through short- or long-range forces derived from chemistry at Harvard macromolecular mechanics (CHARMM) force fields. These force fields are Lennard-Jones (L-J) potentials with variable cutoff distances and widths. These potentials were originally developed to study proteins and other organic/biological molecules. Recent work has focused on determining parameters for silica with CHARMM force fields to enable modeling of silica surfaces with organic and biological molecules. Fully atomistic representations of hexane (C_6H_{14}) including all hydrogen atoms and silica (SiO_2) including, as described below, SiOH surface terminations were used. Simulations were performed using time integration of Nose-Hoover style non-Hamiltonian equations of motion for isothermal-isobaric (NPT) ensembles.

6.2 Simulation of bulk hexane: Simulations of bulk n-hexane were performed by constructing a single n-hexane molecule and then replicating it, typically for a total of 1000 molecules. These molecules were then placed on an artificial 10 x 10 x 10 hexane lattice in a 3-dimensional box with periodic boundary conditions and variable size in all three directions. Simulations were run until the total energy of the system equilibrated. An example at 300 K and 1 bar is shown in Figure 17. Although specified, and on average equal to the specified values, the instantaneous temperature and pressure for each time step varies. In contrast, the total energy shows a monotonic decrease as the configuration of the hexane evolves. In this case, the system was considered equilibrated after ~5000 ps.

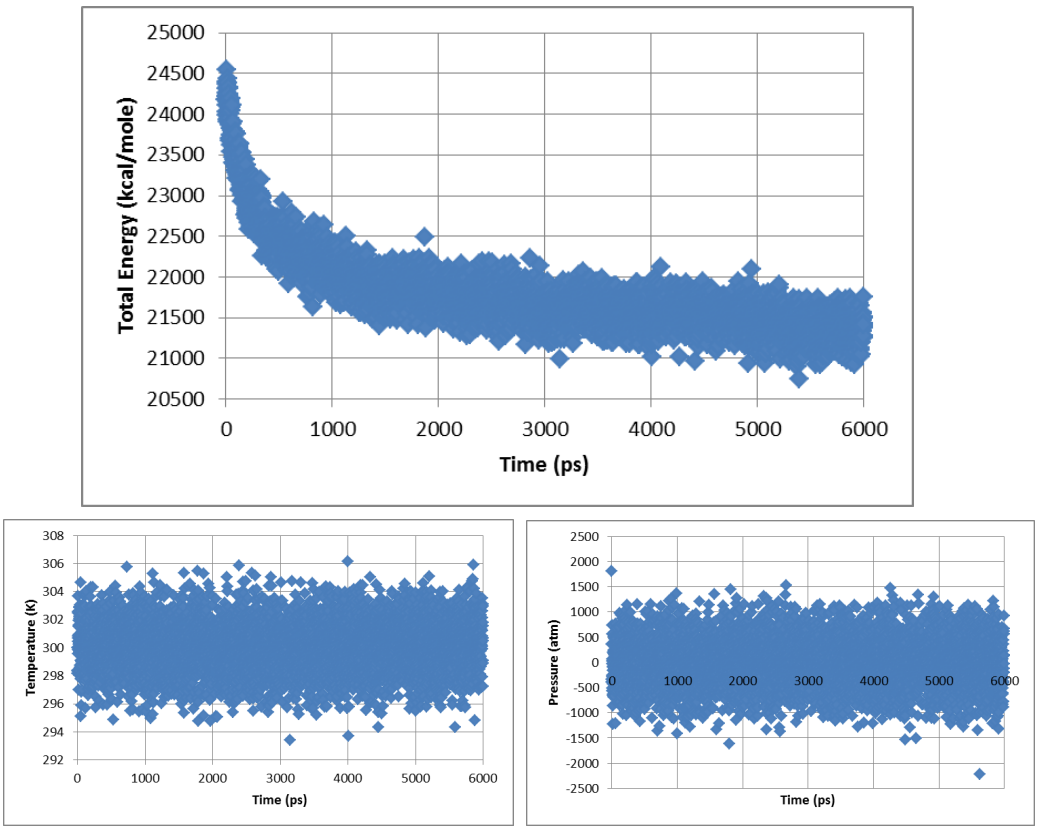

Figure 17. Numerical equilibration of the total energy during molecular dynamics simulation of bulk hexane. The simulation was conducted with 1000 hexane molecules at 300 K and 1 bar in 1 fs time steps with outputs every 1 ps. Total energy (top); temperature and pressure (bottom).

Using harmonic potentials, atoms within individual molecules of hexane were set and bound based on the OPLS (optimized potentials for liquid simulations) all approach.(12) Thus, while the molecules were flexible, no dissociation or chemistry could occur. This restriction was not limiting because only long range, low energy, nonbond-breaking, interactions between molecules are important for the liquid-state hexane studied in this work. Long range interactions are influenced by the tails of the L-J potentials. These tails are specified in CHARMM force fields by cutoff points and cutoff lengths. The cutoff point is the distance at which the L-J dependence ends and the potential begins to decrease to zero. The cutoff length is the width over which this decrease occurs. The functional form of this decrease is specified by CHARMM.

Cutoff points and lengths were determined by fitting to the bulk hexane heat capacity and density, as shown in Figure 18. To determine the heat capacity, system enthalpies were determined at 1 bar from individual simulations at 250 K to 300 K. The dependencies with temperature are well described as linear from which the heat capacity (kJ/mol-K) is given by the slope. A cutoff from 9.5 Å to 11.0 Å gave a heat capacity of 0.216 kJ/mol-K. This cutoff also gave a density at 300 K of 0.68 g/cm^3. These values were judged acceptable compared to experimental values of 0.198 kJ/mol-K and 0.659 g/cm^3.

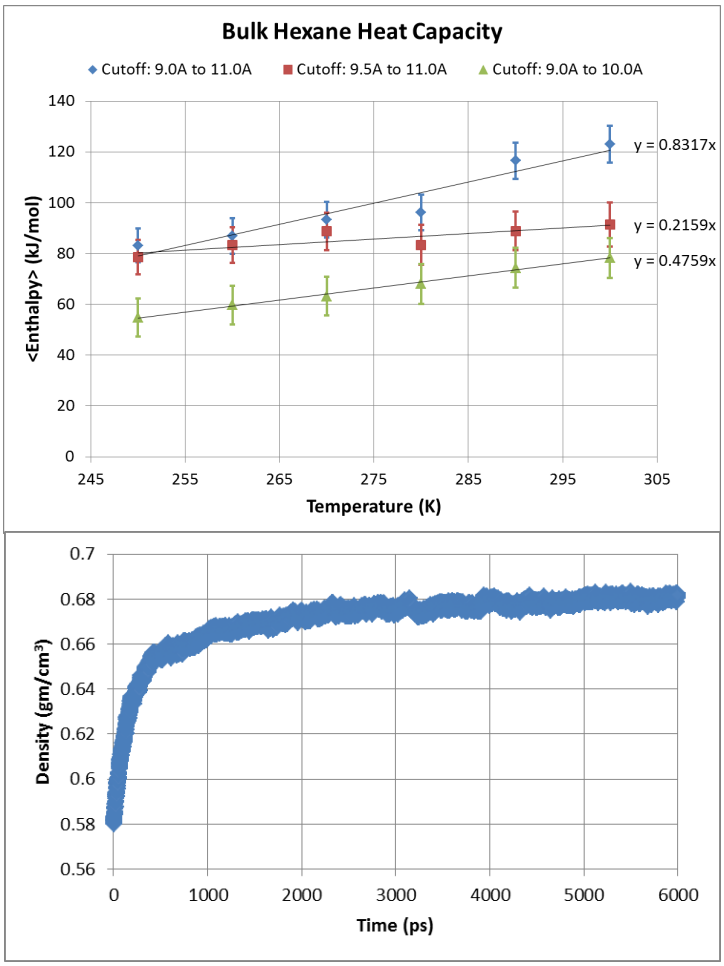

Figure 18. Enthalpy and density evolution of bulk hexane with different L-J potential cutoff points and lengths. The slopes of linear fits to the enthalpy (top) give the heat capacities (as indicated) in kJ/mol-K. For a cutoff of 9.5 Å to 11.0 Å, the density (bottom) equilibrates at 0.68 g/cm^3.

The pair correlation function was also compared with the pair correlation function from a recently published simulation (Figure 19).(13) Except for correlations related to atoms within the same hexane molecule, which are not included in the current analysis, the peaks occur at the same distances indicating good agreement between the two simulations. A typical equilibrated MD simulation configuration for hexane using the fitted cutoff parameters is shown in Figure 20.

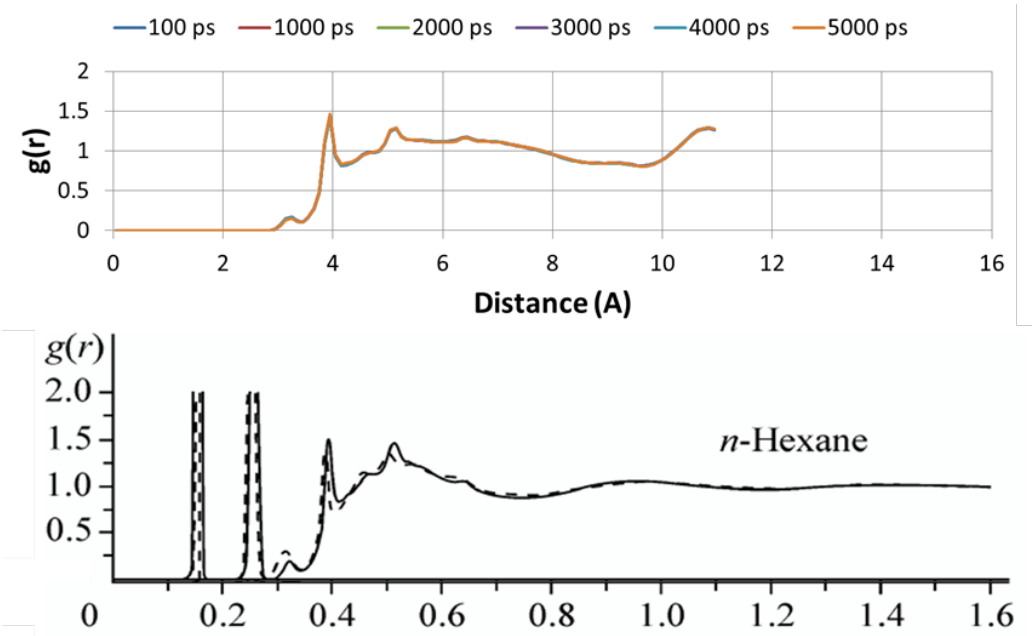

Figure 19. Pair correlation functions, g(r), from MD simulations of bulk hexane at 300 K and 1 bar. Current simulations (top) are well converged after 100 ps, thus, the functions for different times are nearly coincident. Recently published simulation (13) (bottom) includes peaks at 0.15 and 0.26 nm from atoms within the same molecule.

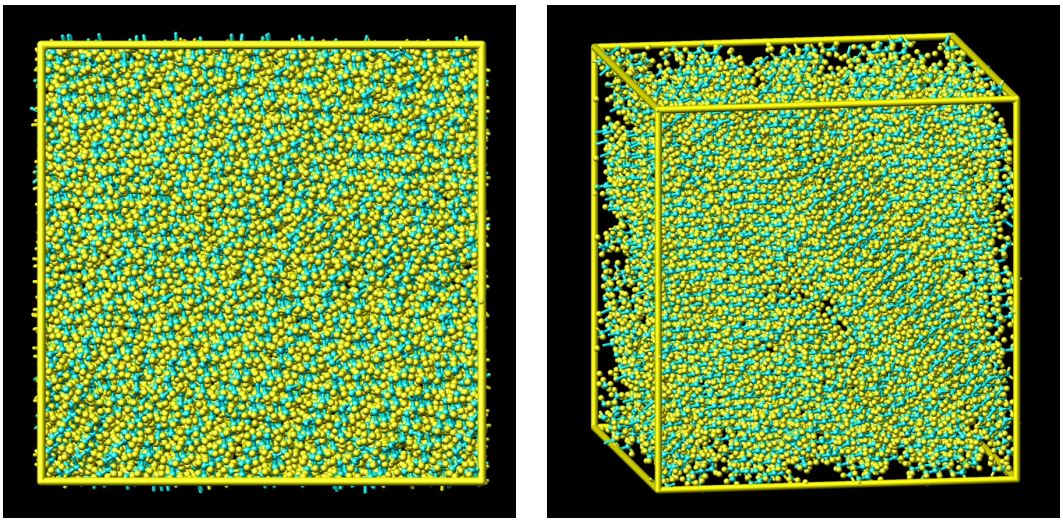

Figure 20. Snapshot of equilibrated molecular dynamics simulation of bulk hexane. Two-dimensional projection (right) and 3-dimensional view (left) following equilibration for ~5000 ps at 300 K and 1 bar. Light blue = carbon; yellow = hydrogen. The volume is 6.12 nm x 5.53 nm x 6.22 nm; it contains 1000 hexane molecules giving a density of 0.68 g/cm^3 = 0.095 atoms/Å^3.

6.3 Simulation of hard wall nano-confined hexane: To bridge simulations of bulk hexane with simulations of hexane confined within a realistic silica pore, hexane was confined in idealized nanopores using perfectly reflecting hard walls in one or two dimensions. A visual comparison of the results for bulk hexane and hexane confined in a 4.5 nm x 4.5 nm hard wall pore is shown in Figure 21. The bulk simulation, which is periodic with variable size in all directions shows a homogeneous distribution of hexane molecules with no apparent ordering, as expected for a bulk liquid. In contrast, hexane nano-confined within fixed hard walls in 2-dimensions spaced 4.5 nm apart clearly shows regions of local ordering. The overall density of hexane in the confined simulations was lower than for the bulk. For the 4.5 nm x 4.5 nm simulation shown in Figure 21, the overall density was 0.588 g/cm^3, a reduction of ~10% compared to the bulk density.

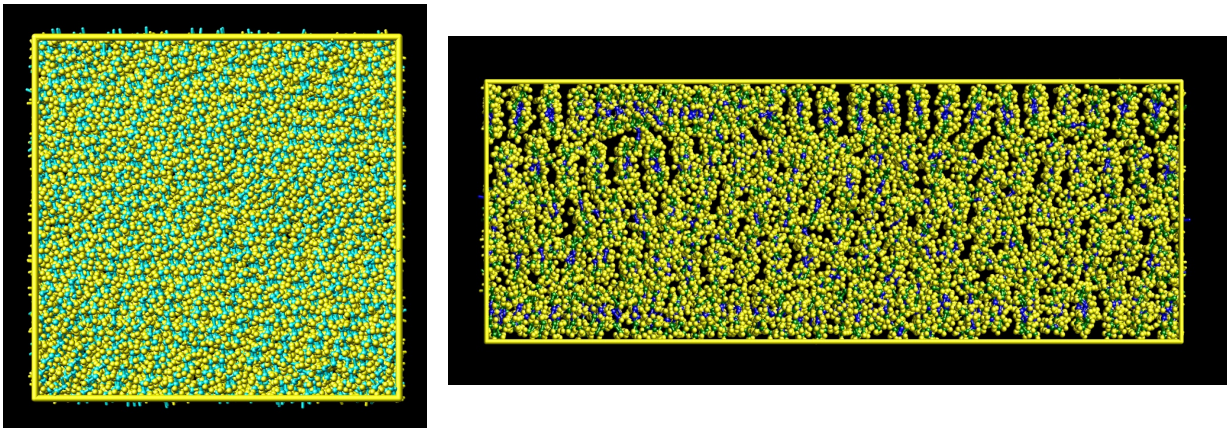

Figure 21. Snapshots of typical configurations for bulk hexane and hexane nano-confined within a square cross section pore with smooth perfectly reflective walls. Both simulations show 2-dimensional projections of equilibrated configurations (1000 molecules) at 1 bar and 300 K. Left: bulk hexane, same as Figure 20 (light blue = carbon; yellow = hydrogen), with variable size and periodic boundaries in 3-dimensions. The simulation box is 6.2 nm square. Right: hexane confined within 4.5 nm x 4.5 nm hard walls in 2-dimensions (blue = CH_2 carbon; green = CH_3 carbon, yellow = hydrogen). The third dimension (elongated, horizontal) is variable and periodic. The bulk simulation is homogeneous with a density of 0.68 g/cm^3. The confined hexane displays localized ordering with an overall density of 0.588 g/cm^3 (~85% of the bulk density).

Equilibrated configurations for hexane confined in 2-dimensions by hard walls 3.5 nm, 4.5 nm, and 7.0 nm apart together with density profiles across one of the confined directions are shown in Figure 22. The number of hexane molecules is fixed for all three simulations so the volume becomes more elongated as the cross section decreases. The 3.5 nm cross-section pore (Figure 22, a-b) shows the most pronounced ordering. The effect decreases for the 4.5 nm pore (Figure 22, d-e) and for 7.0 nm (Figure 22, g-h) the ordering is faint with a nearly bulk like appearance. The ordering seen in the snapshots is also seen in the density profiles (Figure 22, c, f, and i). At 3.5 and 4.5 nm, large oscillations of +30% to -40% around the bulk density (experimental bulk number density = 0.093 atoms/Å^3 = 0.659 g/cm^3) are seen. For 7.0 nm, the oscillations are much smaller, <15%. As shown for the profiles at different simulation times, these oscillations grow in and then stabilize after ~2000 ps. The overall density increased with pore size from 0.578 g/cm^3 for a 3.0 nm x 3.0 nm pore to 0.598 g/cm^3 for a 7.0 nm x 7.0 nm pore. Thus, the density appeared to smoothly transition from ~10% lower than the bulk for the smallest pore size to the bulk density as the pore size reached ~7 nm.

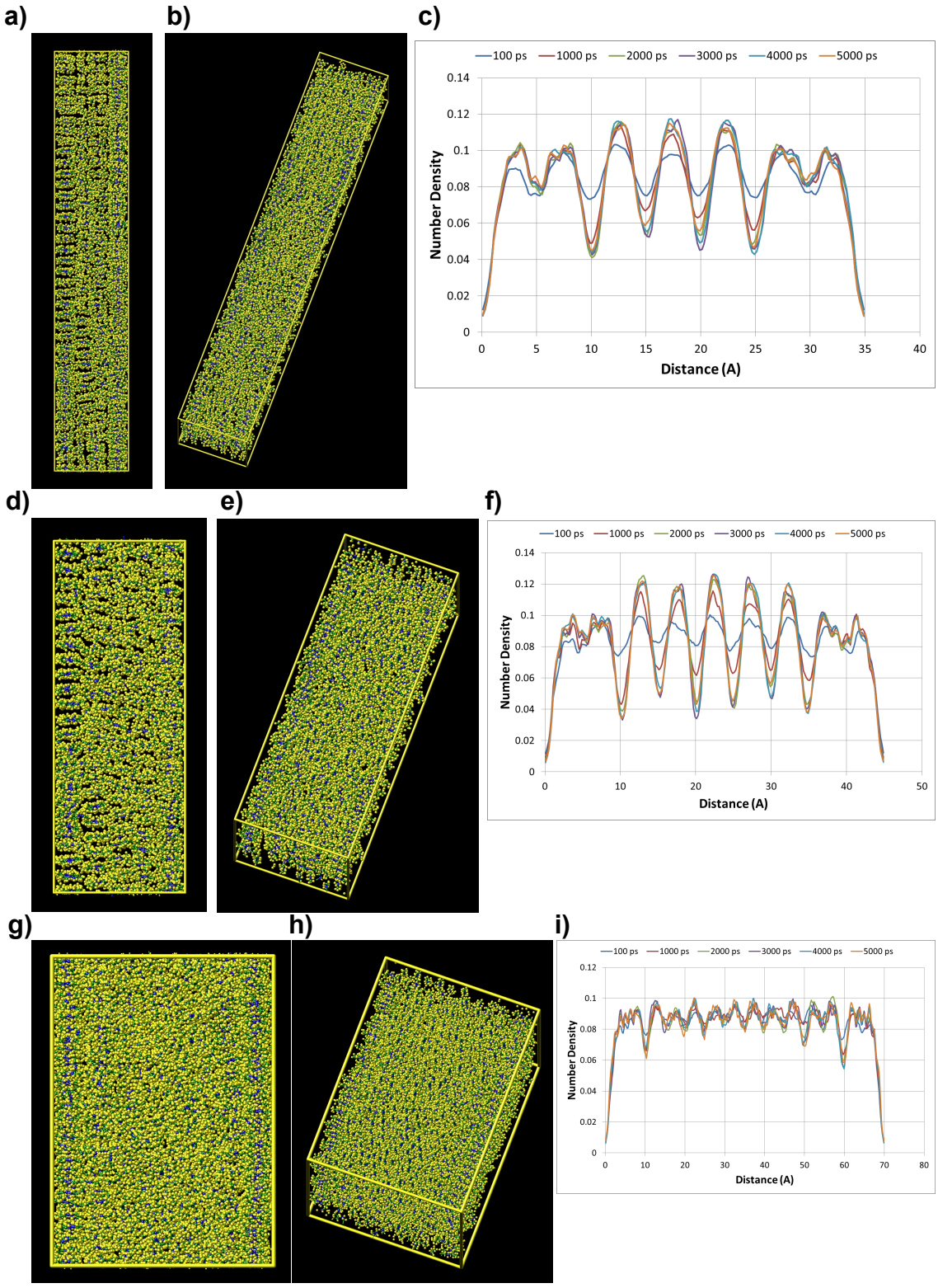

Figure 22. Visualizations and density profiles of hexane confined in square cross section hard wall pores. a – c) 3.5 nm x 3.5 nm; d – f) 4.5 nm x 4.5 nm; g – h) 7.0 nm x 7.0 nm. The 2-dimensional projection in d) is the same projection shown in Figure 21.

The occurrence of solid state-like ordering with a lowered overall density upon nano-confinement is unexpected. Such a result may be an artifact of the perfectly reflective walls. While artifacts were considered and sought-out, the influence of a computational artifact on these results could not be confirmed. To check for artifacts from the initial hexane configuration, high temperature (700 K) simulations were run to fully randomize the configurations. After this step, the temperature was lowered to 300 K. The ordering and density oscillations shown in Figure 22 returned confirming that these effects did not originate from the starting configuration.

Confinement in 2-dimensions in a square cross section box yields sharp 90° corners along the edges of the simulation volume. To check for influence of these corners, a 1-dimensionally confined simulation was run with a 3.5 nm spacing. This slit pore geometry does not contain any corners. Figure 23 shows the results compared to the 2-dimensionally confined 3.5 nm x 3.5 nm simulation. The visualization looks nearly random although the density profile still shows oscillations toward the center of the pore. Thus, the 90° corners may have seeded the localized ordering.

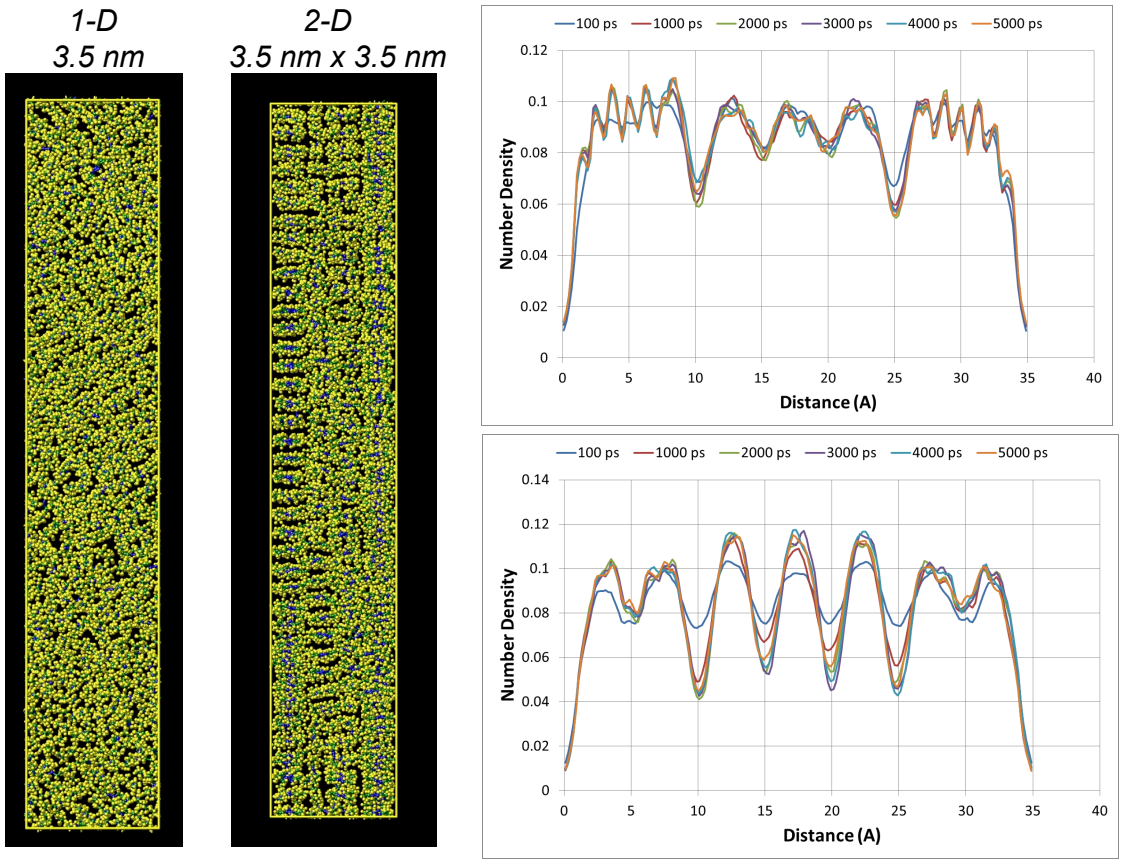

Figure 23. Comparison of 1- and 2-dimensionally confined hexane. Top view projections along confined direction (as labeled, left) and density profiles for 3.5 nm slit pore (right, top) and 3.5 nm x 3.5 nm square cross section pore (right, bottom) geometries.

Although artifacts due to the unrealistic nature of the perfectly hard wall and/or the square cross section pores could not be ruled out, the reduced density seen for most simulations with at least one direction restricted to <~ 7 nm could be a mechanism whereby confinement leads to enhanced gas solubility. Specifically, the lower density, giving a larger molar volume would likely increase the number of sites between hexane molecules where a gas molecule could be solubilized.

6.4 Simulation of silica containing a realistically terminated cylindrical nanopore: Based on published experimental results (2) of enhanced solubility of hydrogen in hexane contained within the cylindrical pore of mesoporous silica MCM-41 (Figure 7) and this project's initial effort to verify these results, a simulation of a fully atomistic silica nanopore was developed. Bulk silica (SiO_2), built up from a unit cell (Figure 24), was first simulated using published bond parameters (14). Agreement of the bond lengths with the experimental and previously simulated bond lengths was used to verify the parameters and the simulation.

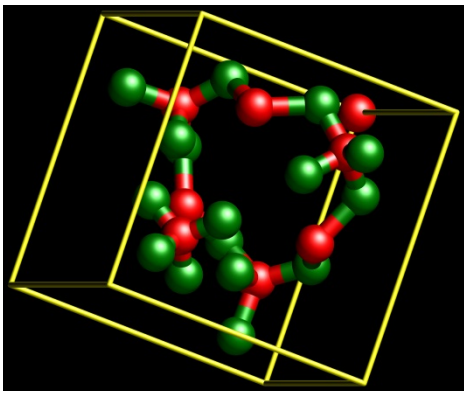

Figure 24. Silica unit cell. Red = silicon; green = oxygen. The edge of the unit cell is 0.7436 nm. This unit cell was used to construct a block of bulk silica from which an ~ 3 nm pore was formed.

Next, as shown in Figure 25, an approximately cylindrical nanopore ~ 3 nm in diameter was formed from a 7.5 nm x 7.5 nm x 7.5 nm block of silica using the procedure described in Ref. 15. Briefly, atoms were manually removed to create the pore. Dangling bonds were terminated with silanol (-Si-OH) or siloxane (-Si-O-Si-) groups statistically according to typical experimentally measured silanol surface concentrations. As shown, silica occupies only about half of the simulation volume in order to create a reservoir for hexane. The flat face of the silica bordering the reservoir was also terminated with silanols and siloxane bridges. After construction of the silica block and formation of the pore, the structure was relaxed under isothermal and isobaric conditions with periodic boundary conditions. Figure 25 shows both the initially ordered and the final relaxed silica configurations together with the reservoir volume. Close inspection of the silica surfaces (best seen in Figure 25 in the top-down views for the pore and the side-on view of the flat surface) indicates that the silanol terminations and the high curvature for the pore lead to a nanoscale roughness with small pockets and protrusions. Thus, these surfaces are significantly different from the smooth hard walled pores.

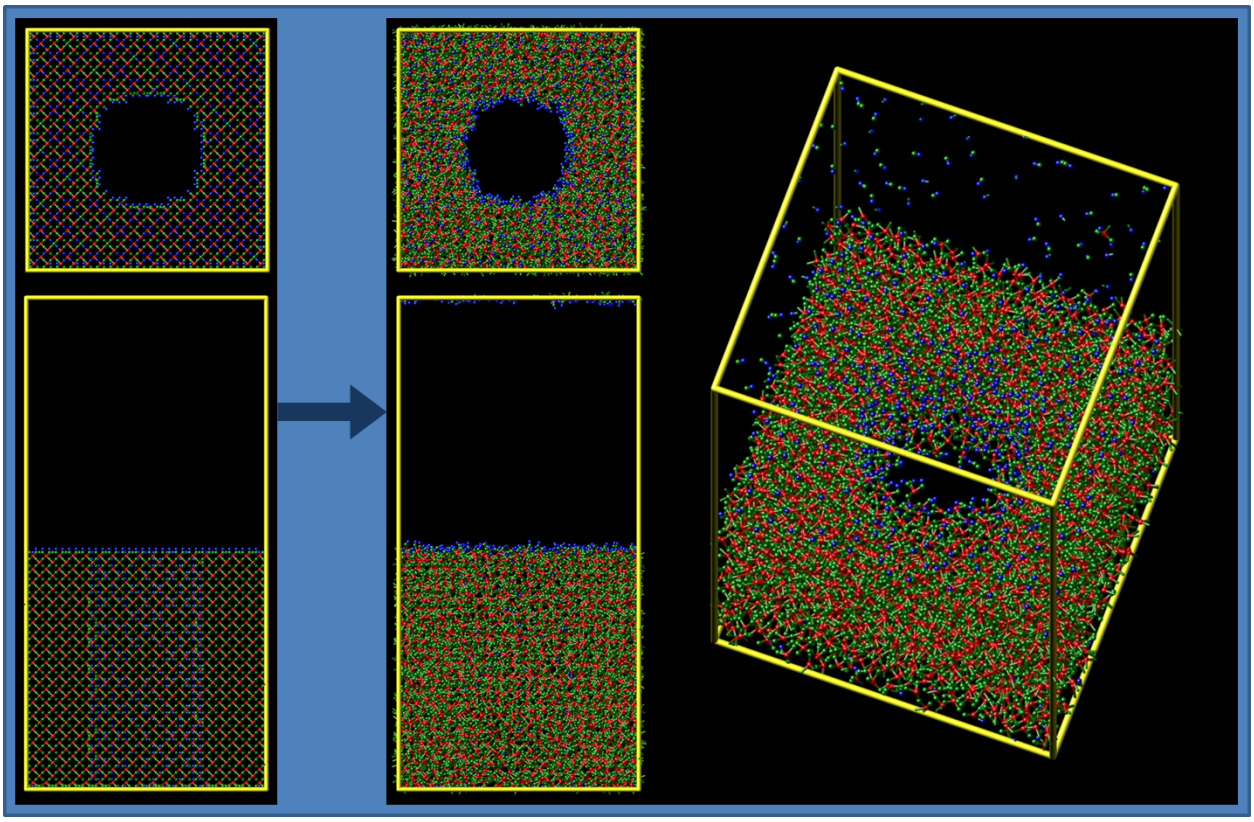

Figure 25. Snapshots of silica pore containing a reservoir for hexane. (left) Initial configuration after constructing pore from silica block with –Si-OH and –Si-O-Si- surface terminations. (center and right) final configuration after relaxation for 2000 ps at 300 K. Silicon (red), oxygen (green) and hydrogen (blue). The width of the volume is 6.7 nm and the diameter of the pore is ~3 nm. The appearance of atoms at the top of the simulation volume after relaxation is due to the periodic boundary conditions coupled with a slight shift in the location of the visualization volume.

6.5 Simulation of bulk hexane interacting with a silica nanopore: Beginning with the equilibrated configuration of the silica nanopore (Figure 25), hexane was added to the reservoir volume and allowed to interact with an initially empty pore. Similar to the bulk hexane simulations, the initial configuration of hexane in the reservoir volume consisted of an artificial lattice. This configuration was equilibrated together with the silica pore, ie, the silica continued to evolve in contact with the hexane, it was not fixed. Figure 26 shows the initial and final configurations together with the hexane densities in the reservoir and in the pore. To be able to understand the distribution of hexane within the pore, the densities were computed for cylindrical shells, 1 Å in width and 4.6 nm long, centered along the center-line of the pore (Figure 26c, inset). The number density of atoms was determined by counting the number of carbon and hydrogen atoms in the volume of the shells as the radius of the shell was increased from 1 Å to 20 Å. The pore wall is at a radius of ~15 Å, although the wall is rough, as described above. The length of the shells spanned a large portion of the pore and the reservoir but avoided the edge of the pore. The final configuration and the density show that the hexane in the reservoir quickly equilibrated to a bulk like condition with a density of ~0.095 atoms/Å^3 independent, as expected, of the shell diameter. However, in contrast, infiltration of hexane into the pore was very slow with only a low maximum density, ~0.02 atoms/Å^3 about half way from the center to the wall and essentially zero in the pore center.

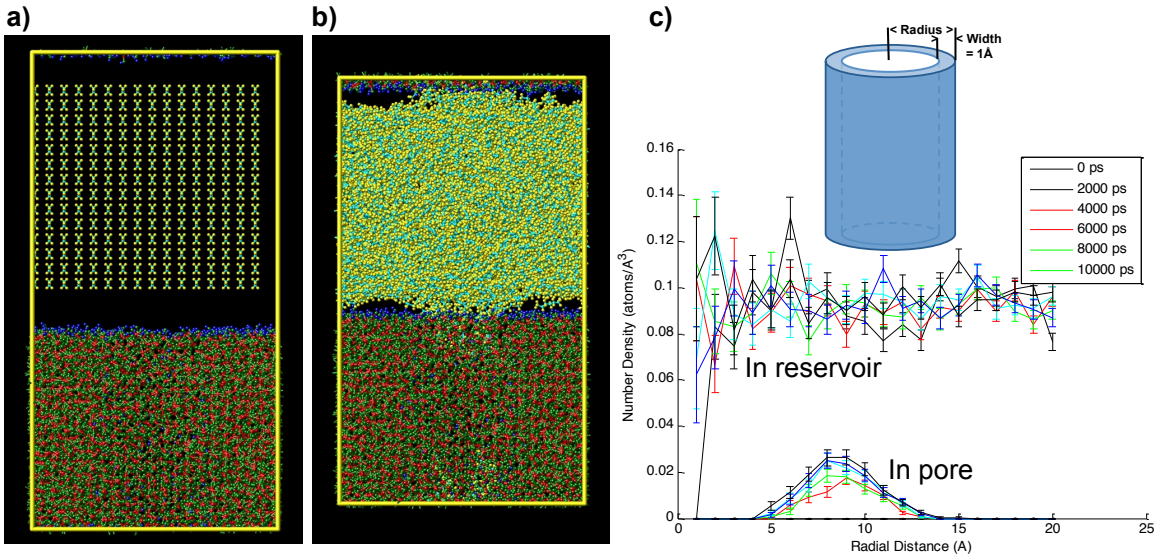

Figure 26. Molecular dynamics simulation of hexane interacting with a silica nanopore. a) Initial configuration starting with an equilibrated silica nanopore, ~3 nm in diameter (from Figure 25), and a reservoir volume containing 1000 hexane molecules arranged in an artificial lattice. The simulation volume is periodic and variable in size in 3-dimensions. b) Final configuration after equilibration for 10,000 ps. Although previously equilibrated, the silica was included in the simulation, it was not fixed. The reservoir equilibrates quickly. However, infiltration into pore and interaction with the silica surface is slow. A few hexane molecules can be seen through the pore wall in the side-view shown. c) Density in the reservoir and pore in 1 Å wide cylindrical shells (shown in inset) as a function of shell radius centered in the pore. The error bars represent counting statistics, $N^{1/2}/V$ where N is the number of atoms in the shell and V is the volume.

The low density within the pore could be an issue of kinetics or it could indicate that the equilibrium density of hexane in the pore is lower than the bulk. If the low density originated from the kinetics, achieving equilibrium would take too long for the available simulation capabilities. To circumvent this limitation, simulations were started from the final configuration shown in Figure 26 but with the few hexane molecules in the pore removed and replaced with a pre-equilibrated cylinder of hexane, ~2.5 nm in diameter. The initial and final configurations and density profiles are shown in Figure 27. As seen for the density profile at 0 ps, the hexane initially filled the center of the pore at approximately the bulk density. Near the pore wall the density decreased (from ~10 Å to 15 Å radius) because any hexane molecules that initially intersected with atoms of the pore were removed. For this simulation, the hexane molecules placed in the pore quickly spread out radially to the walls of the pore, again forming a low-density region in the center of the pore. Additional molecules are seen moving into the pore.

At this point it was still uncertain whether the low density in the pore represented a kinetic limitation, an equilibrium condition, or an artifact of the calculation. To try further to understand this behavior, the final configuration from the simulation in Figure 27 was continued at temperatures of 300 K, 400 K, 500 K, and 700 K for 10,000 ps. The higher temperatures were used to enhance the kinetics for the hexane to infiltrate the silica pore. The density profiles from those simulations are shown in Figure 28. At 300 K almost no change occurs. This was as expected given that almost no change occurred in the previous 1000 ps, as shown in Figure 27.

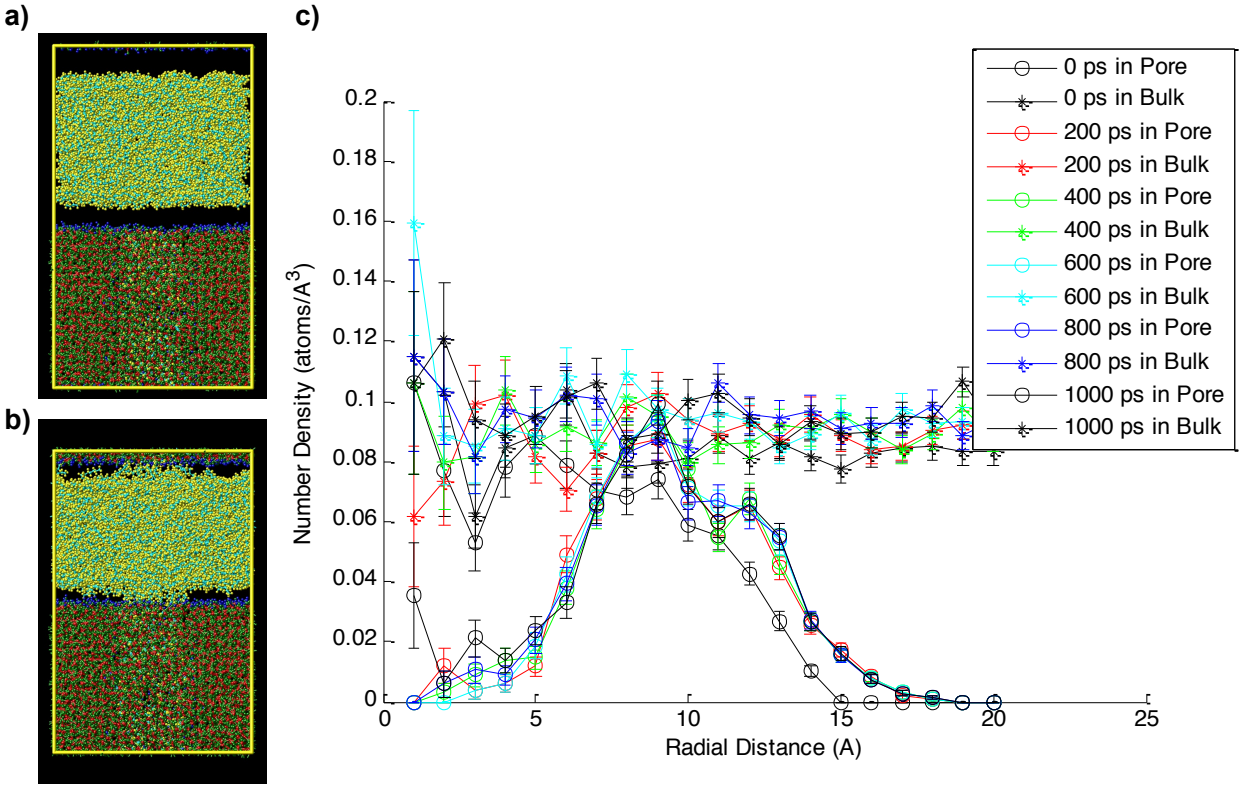

Figure 27. Configurations and density profile for hexane in silica nanopore. a) Initial configuration with hexane placed in the pore (as described in the text). b) After equilibration at 300 K for 1000 ps. c) Density profiles in the (bulk) reservoir and in the pore including the starting profile (0 ps).

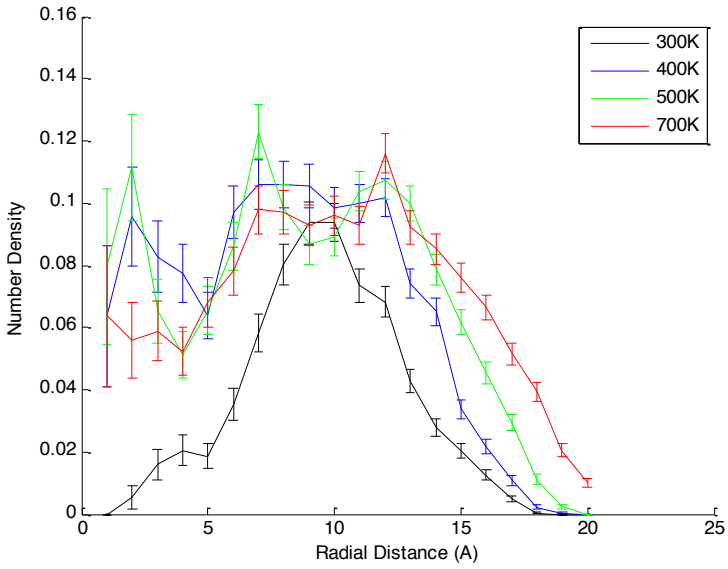

Figure 28. Density profiles for hexane in silica nanopore after high temperature equilibration. Starting from the final configuration shown in Figure 27, the simulation was run for an additional 10,000 ps at 300 K, 400 K, 500 K, and 700 K. Resulting radial cylindrical shell density profiles for hexane in the pore are as shown. For comparison, the bulk density is ~0.095 atoms/Å^3.

In contrast, significant filling-in of the center of the pore up to a density of ~ 0.08 atoms/Å^3 is seen at the higher temperatures. This indicates that the low density in the center of the pore is likely not an equilibrium condition but rather the result of slow kinetics. The equilibrium density may still be somewhat lower than the bulk but, judging from the profiles in Figure 28 (at < 5 Å), it is probably at least > 0.08 atoms/Å^3. This density is < 15% lower than the bulk density. As described above for the hard wall confinement simulations, a density decrease of 10-15% could be a mechanism for enhanced gas solubility. However, given the slow equilibration, the simulations are not able to accurately resolve density differences < 15%.

Clearly, within these simulations, the approach to equilibrium in the pore is much slower than in the bulk. The kinetics may be slow because the first hexane molecules that enter the pore adsorb onto the pore walls. These adsorbed hexane molecules are relatively immobile. This first layer of adsorbed hexane is ~ 8 Å thick. This layer restricts infiltration of additional hexane to a diameter of ~15 Å, which is small enough, ~2 molecular lengths, to be slow.

In addition, the density profiles in Figure 28 also show that the density near the pore wall (from ~12 Å to 20 Å) fills in at higher temperatures. This filling-in indicates that at 300 K the first hexane molecules to infiltrate the pore and adsorb on the pore walls become immobile (or kinetically locked) before they fully (or optimally) fit into the roughness of the wall. The motion of molecules adsorbed on the wall is essentially frozen (over ~ 10,000 ps) at 300 K while at higher temperatures the kinetic barriers to motion are overcome. For example, the density at 15 Å radius increases from 0.02 atoms/Å^3 at 300 K to 0.08 atoms/Å^3 at 700 K. To the extent that these simulations relate to experimental measurements, the kinetic difficulty in obtaining an optimally configured adsorbed solvent layer could by a mechanism whereby adsorbed gas (hydrogen) capacity is retained in nano-confined solvent/nanoporous scaffold composites.

While still not complete, overall, these simulations suggest that compared to a bulk environment, the interaction of hexane with an ~3 nm diameter cylindrical silica pore is kinetically inhibited. This inhibition is manifest in two ways. First, the hexane molecules adsorbed on the pore wall become locked before optimal packing is achieved. Second, the locking of this layer restricts filling of the remaining central portion of the pore.

6.6 Interaction of hydrogen with hexane confined within a silica nanopore: Although simulations to directly determine the enhanced solubility of hydrogen in nano-confined hexane were not completed, the interaction of hydrogen with configurations resulting from hexane infiltration into a 3 nm silica pore was briefly studied. Determining absolute hydrogen solubilities requires a thermodynamic reservoir, as described above for hexane. Instead, using available simulations, the relative interaction of hydrogen with bulk hexane and hexane in the pore was examined. A chosen number of hydrogen molecules were placed in the bulk hexane reservoir. For this brief study, H_2 molecules were simulated as single spheres.(16) The redistribution of these hydrogen molecules was monitored as the hexane and silica were further equilibrated. Two simulations were run at 300K. The first simulation started with hexane in the silica pore equilibrated at 400 K. As shown in the density profile in Figure 28, after 10,000 ps at 400 K the hexane density in the center of the pore had largely filled in while the density near the pore wall was only partially filled. The second simulation started with configuration equilibrated at 700 K. The density profile for this simulation (Figure 28) shows considerable filling-in of hexane near the pore wall. Beginning with these configurations, both simulations were run at 300 K for 10,000 ps. The starting and final configurations and the hydrogen molecule location and density profiles are shown in Figures 29 and 30.

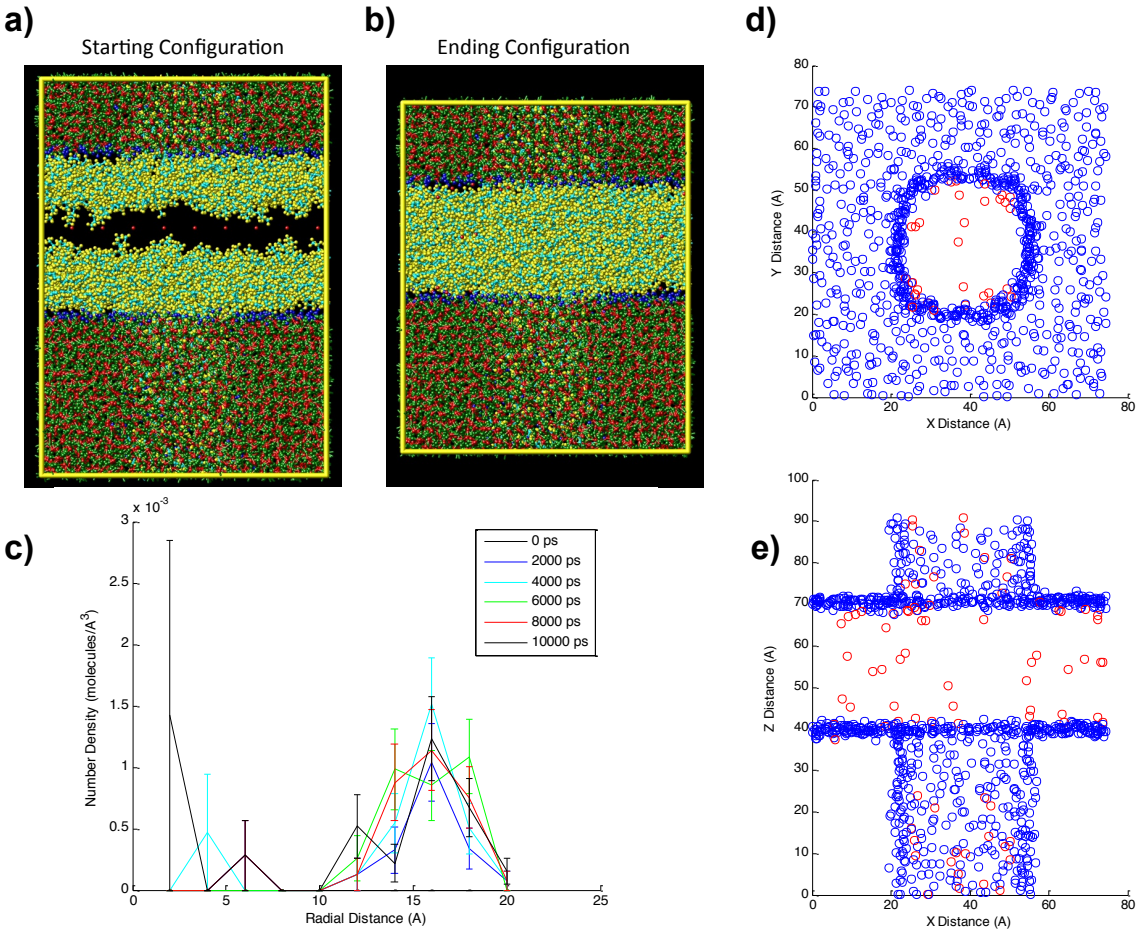

Figure 29. Hydrogen interaction with hexane in silica nanopore previously equilibrated at 400 K. a) Starting configuration from the simulation at 400 K with the hexane density profile shown in Figure 28. Molecular hydrogen was introduced into the reservoir by removing hexane to create a free space and adding 81 H_2 molecules arranged on an artificial square lattice, seen edge-on. For the 857 total hexane molecules in the simulation, this corresponds approximately the solubility of hydrogen in bulk hexane at 100 bar. Thus, the simulations were run at 100 bar. b) Final configuration after equilibration for 10,000 ps at 300 K. The free space quickly collapses and the hydrogen is dispersed into the hexane. c) Density profile (in 1 Å wide cylindrical shells) for hydrogen in the silica pore. d) Final configuration top-down view showing hydrogen atoms in surface silanol groups (blue) and hydrogen molecules (red) in the pore only. e) Side-on view showing hydrogen atoms in silanol groups (blue) and hydrogen molecules (red) in both the pore and the reservoir.

For the simulation based on the 400 K starting configuration (Figure 29), the hydrogen molecules quickly mixed throughout the hexane (Figure 29e) and populated the open adsorption sites on the walls of the pore. Figure 29c shows a peak in the density profile near the pore wall at ~16 Å radius. These adsorbed hydrogen molecules can also be seen in the top-down view of the final configuration shown in Figure 29d, which shows only hydrogen molecules in the pore. For the 700 K starting configuration, the result is similar although there are many fewer

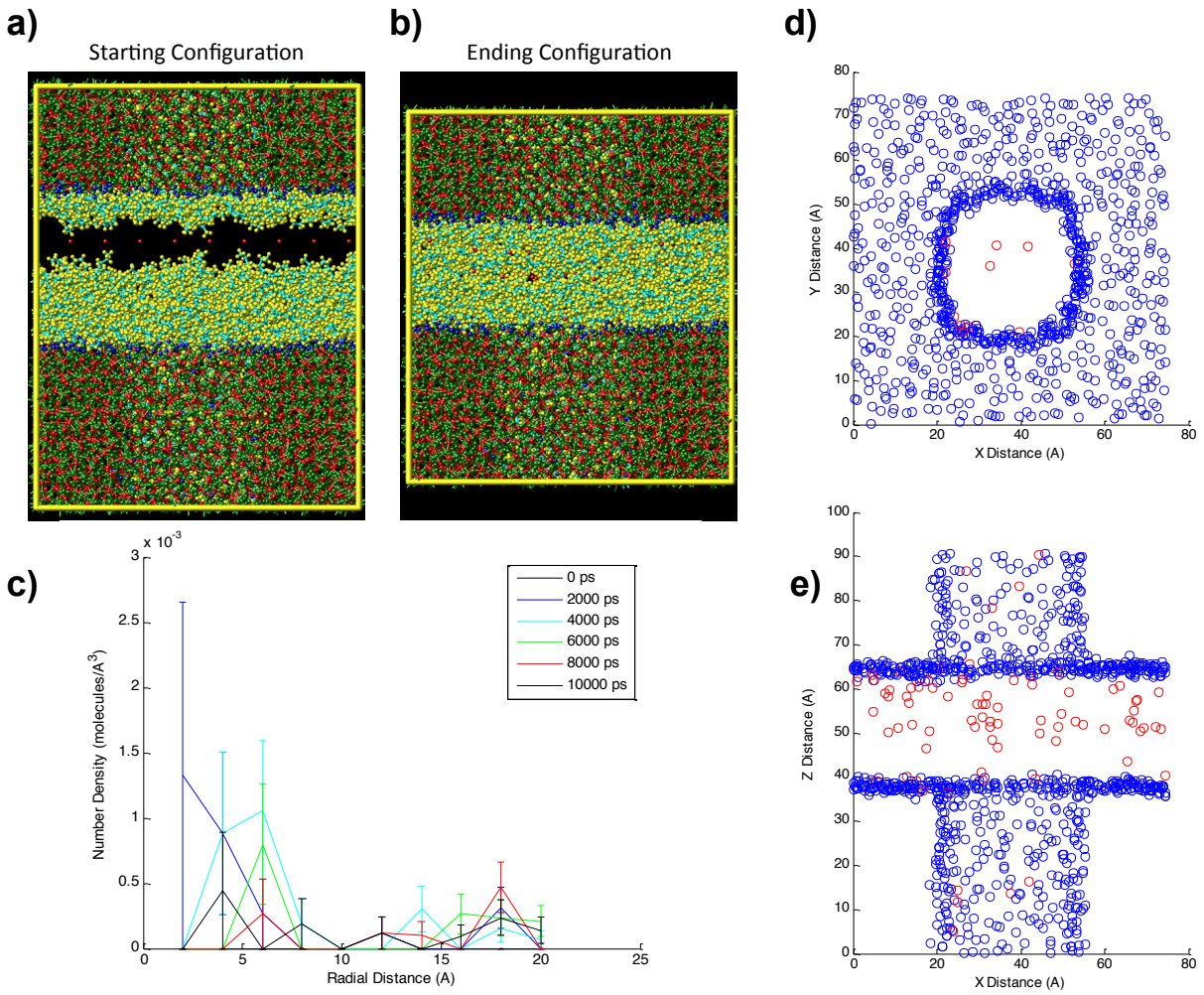

Figure 30. Hydrogen interaction with hexane in silica nanopore equilibrated at 700 K. a) Starting configuration from the simulation at 700 K with the hexane density profile shown in Figure 28. Molecular hydrogen was introduced into the reservoir by removing some hexane to create a free space and adding 81 H_2 molecules arranged on an artificial square lattice, seen edge-on. For the 862 total hexane molecules in the simulation, this corresponds approximately the solubility of hydrogen in bulk hexane at 100 bar. Thus, the simulations were run at 100 bar. b) Final configuration after equilibration for 10,000 ps at 300 K. The free space quickly collapses and the hydrogen is dispersed into the hexane. c) Density profile (in 1 Å wide cylindrical shells) for hydrogen in the silica pore. d) Final configuration top-down view showing hydrogen atoms in surface silanol groups (blue) and hydrogen molecules (red) in the pore only. e) Side-on view showing hydrogen atoms in silanol groups (blue) and hydrogen molecules (red) in both the pore and the reservoir.

hydrogen molecules adsorbed along the pore wall because of the higher density, better packed, hexane (Figure 28). The peak in the density profile from the 400 K configuration (Figure 29c) is nearly gone in the profile from the 700 K configuration (Figure 30c). As a result of the many fewer hydrogen molecules adsorbed along the pore wall, there are more molecules remaining in the reservoir (compare Figures 29e and 30e). These results substantiate the speculation above that the kinetically limited incomplete packing of hexane molecules along the pore wall could be a mechanism for retained hydrogen capacity.

The approximately cylindrical, 3 nm diameter, pore discussed above is confined in 2-dimensions. In contrast, the flat surfaces bounding the hexane reservoir may be considered as a model of a slit pore confined in 1-dimension with a width of ~2.5 nm to 3 nm (see dimensions from Figures 29e and 30e). Although constructed initially only out of necessity to form the hexane reservoir, the (adsorbed) hydrogen molecule density along this 1-dimensionally confined space can be compared with the (adsorbed) density in the 2-dimensionally confined cylindrical pore. A comparison of these areal densities (H_2 molecules/Å^2) is shown in Figure 31.

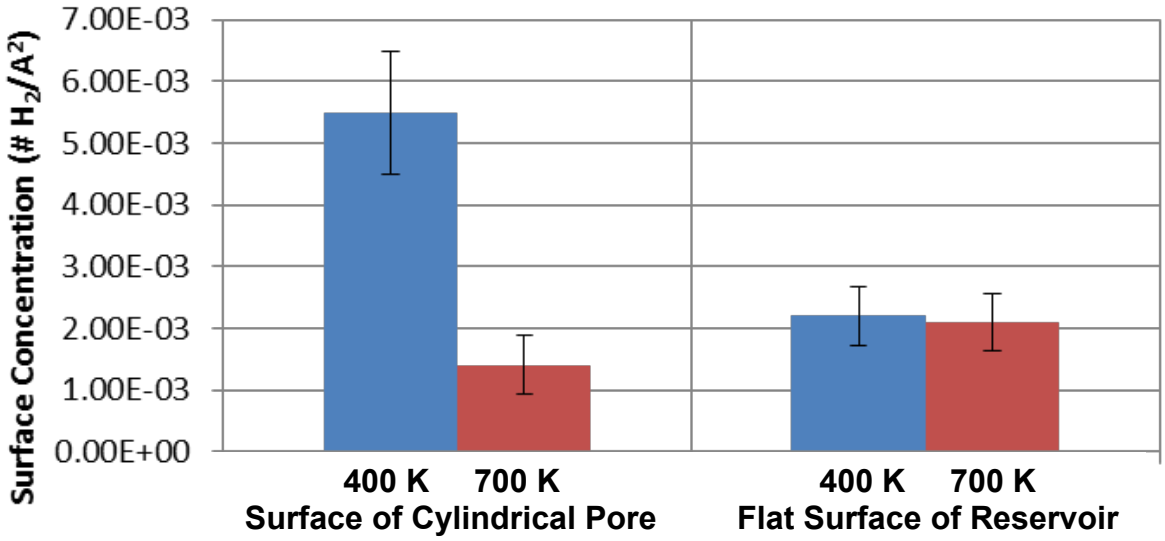

Figure 31. Adsorbed hydrogen areal molecular densities at 300 K for 1- and 2-dimensionally confined pores containing hexane. Densities were determined from the simulations shown in Figures 29 and 30. The cylindrical pore (left) is 2-dimensionally confined while the flat surface of the hexane reservoir (right) is 1-dimensionally confined. The temperatures indicate the equilibration temperatures for the hexane. Hydrogen molecules were considered adsorbed if they were within 0.5 nm of an oxygen or silicon atom. The error bars represent counting statistics, $N^{1/2}/A$ where N is the number of adsorbed hydrogen molecules and A is the surface area.

As discussed above, in the cylindrical pore the hydrogen density is high for the 400 K configuration because the hexane molecules are inhibited from optimally packing along the pore wall by the 2-dimensional confinement. Equilibrating the hexane at 700 K overcomes this barrier and the sites for hydrogen adsorption are fewer. In contrast, on the flat surface of the reservoir, which is only confined in 1-dimension, the hexane molecules are able to pack well even at 400 K and therefore, the number of sites for hydrogen is low. In fact, the areal hydrogen concentrations are equal for the 400 K and 700 K configurations and also approximately equal to the concentration for the 700 K configuration in the cylindrical pore. Thus, when the hexane can optimally pack, the remaining sites for hydrogen are similar for both surfaces. The difference between the surfaces originates from the dimensionality of the pore. Two-dimensional confinement leads to more inhibition of the hexane, which leads to more sites for hydrogen adsorption. Interaction of hexane with a flat, 1-dimensionally confined pore, is less restrictive leaving less sites for subsequent hydrogen adsorption.

This comparison between the cylindrical pore and the flat surface is relatable to the comparison between the carbon aerogel and activated carbon scaffolds discussed above in Section 5.8. For

several solvents, the retained hydrogen capacity in carbon aerogel was consistently higher than in activated carbon (Figure 16). Based on the simulation results, this difference in retained hydrogen capacity may result from the more restricted movement of solvent within the 3-dimensionally confined pores of the carbon aerogel compared to the 2-dimensionally confined (slit) pores of the activated carbon. Moreover, the geometry appears to be more important than the actual pore size considering that the mode (most probable) pore size for the aerogel is ~5 nm, while the activated carbon is smaller, ~ 2 nm.

In addition to hydrogen molecules adsorbed on the silica surfaces, there are also hydrogen molecules in the center of the pore. The simulations focused on hexane infiltrating the pore indicated that filling in the center of the pore was kinetically restricted. To assess how this restriction affected the interaction with hydrogen, the volumetric densities of hydrogen within the pore and within the reservoir (but excluding adsorbed hydrogen) were compared. The results are shown in Figure 32.

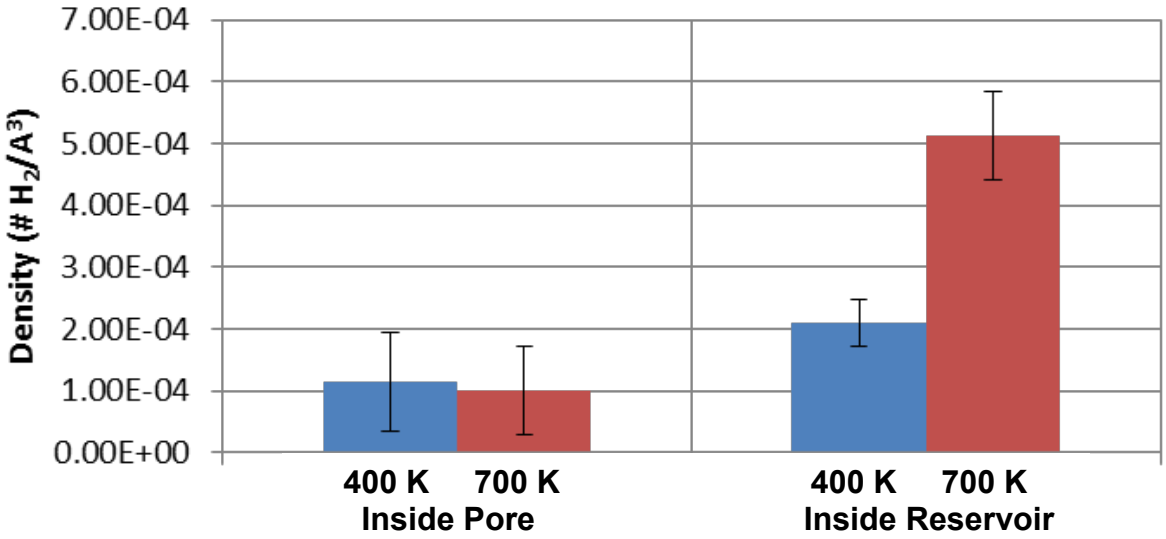

Figure 32. Hydrogen molecular densities at 300 K in hexane contained within a 3 nm diameter pore and in a reservoir volume. Densities were determined from the simulations shown in Figures 29 and 30. The temperatures indicate the equilibration temperatures for the hexane. Hydrogen molecules were considered inside the pore or inside the reservoir if they were > 0.5 nm from an oxygen or silicon atom of the scaffold. The error bars represent counting statistics, $N^{1/2}/V$ where N is the number of adsorbed hydrogen molecules and V is the volume.

The hydrogen density inside the pore is lower than in the reservoir. This lower density occurs despite the somewhat lower density of hexane in the pore, as seen in Figure 28. An early hypothesis for this project was that altering the structure of the solvent by confinement might lead to enhanced gas solubility. The results from these (very limited) simulations appear to show a decrease. The origin for this decrease may be related to the packing of the hexane molecules within the pore. As seen in Figure 28, for the first adsorbed layer at approximately one hexane molecular length (~ 8 Å, Figure 7), from the pore wall the density is > 0.1 atoms/Å^3, slightly exceeding the bulk density of 0.095 atoms/Å^3. This higher density may exclude hydrogen leading to the minima in the hydrogen density profiles at ~8 Å to 10 Å radius seen in Figures 29c and 30c. Any increase nearer to the center of the pore is insufficient to overcome the exclusion from the first adsorbed layer.

7. Conclusions: Although additional work (as described below) directed at both characterizing and optimizing hydrogen uptake (enhanced solubility) in nano-confined solvent/nanoporous scaffold composites would be useful, the combined experimental and computational work in this project strongly suggest that hydrogen storage based on enhanced solubility in solvents confined within porous scaffolds will not yield practical hydrogen storage materials capable of meeting the DOE goals.

Specifically, volumetric measurements of the room temperature hydrogen uptake at pressures from ~10 bar to 150 bar on a variety of confined solvent/porous scaffold composites indicate that a significant fraction of the hydrogen capacity of the empty scaffold can be retained, when the capacity is expressed on a volumetric basis relative to the pore volume of the scaffold (the pore volume-volumetric capacity). Retained capacities up to ~70% relative to empty scaffolds were demonstrated. However, capacities >100%, meaning that more hydrogen is stored in the composite than in the empty scaffold, are required for any composite to be practical for hydrogen storage. High, retained, capacities are facilitated by 3-dimensionally confined pore geometries and increased size of the incorporated solvent molecules. Achieving a capacity >100% seems unlikely, although such capacities maybe possible with exceptionally large solvent molecules.

The retained capacity appears to be associated with hydrogen contained within solvent-filled pores, as opposed to hydrogen simply adsorbing in empty pores too small to admit solvent molecules. While the exact mechanism is uncertain, fully atomistic molecular dynamics simulations of hexane interacting with a 3 nm diameter silica pore indicate that restricted movement of hexane molecules within the pore inhibit optimal packing of the first layer of hexane on the pore walls. This inhibition leaves open sites for hydrogen adsorption on the pore wall despite hexane filling the pore.

8. Future work: The experimental measurements performed in this project quantified but did not characterize the hydrogen capacity of nano-confined solvent/nanoporous scaffold composites. To validate the mechanisms of retain hydrogen capacity suggested by the molecular dynamics simulations, *in-situ* characterization of hydrogen in the composites would be valuable. This characterization could be accomplished using any techniques able to probe hydrogen molecules and determine their immediate environment; in particular, distinguishing whether they are adsorbed on the scaffold pore walls or surrounded by solvent molecules. Simulations that include hydrogen in contact with a thermodynamic reservoir would also serve to quantify the relative interactions explored in the limited preliminary study conducted in this project.

In addition, to better understand whether a pore volume-volumetric capacity greater than the empty scaffold capacity is possible, it would be insightful to study a series composites based on a selected scaffold and a suit of solvents where the solvent sizes span the pore sizes of the scaffold. Such a study could reveal whether the retain capacity asymptotically approaches 100% or might be able to exceed 100%.

9. References

1. E. Brunner, Solubility of hydrogen in 10 organic solvents at 298.15, 323.15, and 373.15 K, *J. Chem. Eng. Data*, **30**, 269-373 (1985).

2. V. Rakotovao, R. Ammar, S. Miachon, M. Pera-Titus, Influence of the mesoconfining solid on gas oversolubility in nanoliquids, *Chem. Phys. Lett.*, **485**, 299-303 (2010).

3. M. Pera-Titus, R. El-Chahal, V. Rakotovao, C. Daniel, S. Miachon, J.-A. Dalmon, Direct volumetric measurement of gas oversolubility in nanoliquids: beyond Henry's law, *Chem. Phys. Chem.,* **10**, 2082-2089 (2009).

4. S. Maichon, V. V. Syakaev, A. Rakhatullin, M. Pera-Titus, S. Caldarelli, J.-A. Dalmon, Higher gas solubility in nanoliquids? *Chem. Phys. Chem.,* **9**, 78-82 (2008).

5. J. J. Vajo, F. Mertens, C. C. Ahn, R. C. Bowman Jr., B. Fultz, Altering hydrogen storage properties by hydride destabilization through alloy formation: LiH and MgH_2 destabilized with Si, *J. Phys. Chem. B,* **108**, 13977-13983 (2004).

6. S. Clauzier, L. N. Ho, M. Pera-titus, B. Coasne, D. Farrusseng, Enhanced H_2 uptake in solvents confined in mesoporous metal-organic framework, *J. Am. Chem. Soc.,* **134**, 17369-17371 (2012).

7. www.acsmaterial.com

8. http://www.gsaresources.com/pdsZS500a.htm

9. http://mkt-intl.com/materials/aerogel/rf-organic-nanofoams/)

10. See Table 3 in (http://www.sigmaaldrich.com/chemistry/chemical-synthesis/learning-center/technical-bulletins/al-1430/molecular-sieves.html).

11. http://lammps.sandia.gov/

12. https://sites.google.com/site/akohlmey/software/topotools/topotools-tutorial---part-2 and reference therein.

13. A. V. Anikeenko, A. V. Kim, N. N. Medvedev, Molecular dynamics simulation of the structure of C6 alkanes, *J. Struct. Chem.,* **51**, 1090-1096 (2010).

14. P. E. M. Lopes ,V. Murashov , M. Tazi , E. Demchuk , A. D. MacKerell , Jr., Development of an empirical force field for silica: Application to the quartz water interface, *J. Phys. Chem. B*, **110**, 2782-2792 (2006).

15. B. Coasne, J. T. Fourkas, Structure and dynamics of benzene confined in silica nanopores, *J. Phys. Chem. C*, **115**, 15471-15479 (2011).

16. F. Salles, D. I. Kolokolov, H. Jobic, G. Maurin, P. L. Llewellyn, T. Devic, C. Serre, G. Ferey, Adsorption and diffusion of H_2 in the MOF type systems MIL-47(V) and MIL-53(Cr): A combination of mocrocalorimetry and QENS experiments with molecular simulations, *J. Phys. Chem. C*, **113**, 7802-7812 (2009).

10. Bibliography

In addition to the specific references given above, the following papers pertain to and were used for this project.

Additional papers from the CNRS group:

1. M. Pera-Titus, S. Miachon, J.-A. Dalmon, Increased Gas Solubility Nanoliquids: Improved Performance in Interfacial Catalytic Membrane Contactors, *American Institute of Chemical Engineers Journal*, **55**, 434 (2009).

2. L. N. Ho, S. Clauzier, Y. Schuurman, D. Farrusseng, B. Coasne, Gas Uptake in Solvents Confined in Mesopores: Adsorption versus Enhanced Solubility, *J. Phys. Chem. Lett.*, **4**, 2274-2278 (2013).

3. S. Clauzier, L. N. Ho, M. Pera-Titus, D. Farrusseng, B. Coasne, Enhanced H_2 Uptake of n-Alkanes Confined in Mesoporous Materials, *J. Phys. Chem. C*, **118**, 10720–10727 (2014).

Papers concerning confined liquids:

4. L. Cheng, J. A. Morrone, B. J. Berne, Structure and Dynamics of Acetonitrile Confined in a Silica Nanopore, *J. Phys. Chem. C*, **116**, 9582-9593 (2012).

5. A. Ghoufi, I. Hureau, D. Morineau, R. Renou, A. Szymczyk, Confinement of *tert*-Butanol Nanoclusters in Hydrophilic and Hydrophobic Silica Nanopores, *J. Phys. Chem. C*, **117**, 15203-15212 (2013).

6. A. Ghoufi, I. Hureau, R. Lefort, D. Morineau, Hydrogen-Bond-Induced Supermolecular Assemblies in a Nanoconfined Tertiary Alcohol, *J. Phys. Chem C*, **115**, 17761-17767, (2011).

7. T. Ueda, K. Kurokawa, Y. Kawamura, K. Miyakubo, T. Eguchi, NMR Study of Molecular Motion of Benzene and *n*-Decane Confined in the Nanocavities of Metal – Organic Frameworks, *J. Phys. Chem. C*, **116**, 1012-1019 (2012).

8. C. L. Jackson, G. B. McKenna, The melting behavior of organic materials confined in porous solids, *J. Chem. Phys.*, **93**, 9002-9011 (1990).

9. D. Morineau, Y. Xia, C. Alba-Simionesco, Finite-size and surface effects on the glass transition of liquid toluene confined in cylindrical mesopores, *J. Chem. Phys.*, **117**, 8966-8972 (2002).

10. P. K. Ghorai, Conformational Preferences of *n*-Butane Inside Zeolite NaY: Comparison of Other Related Properties with *iso*-Butane, *J. Phys. Chem. B*, **114**, 6492-6499 (2010).

11. Y. Xu, T. Watermann, H-H. Limbach, T. Gutmann, D. Sebastiani, G. Buntkowsky, Water and small organic molecules as probes for geometric confinement in well-ordered mesoporous carbon materials, *Phys. Chem. Chem. Phys.*, **16**, 9327-9336 (2014).

12. N. N. Rajput, J. Monk, R. Singh, F. R. Hung, On the Influence of Pore Size and Pore Loading on Structural and Dynamical Heterogeneities of an Ionic Liquid Confined in a Slit Nanopore, *J. Phys. Chem. C*, **116**, 5169-5181 (2012).

13. E. J. Kintzel, Jr., M. K. Kidder, A. C. Buchanan, III, P. F. Britt, E. Mamontov, M. Zamponi, K. W. Herwig, Dynamics of 1,3-Diphenylpropane Tethered to the Interior Pore Surfaces of MCM-41, *J. Phys. Chem. C*, **116**, 923-932 (2012).

14. X. Yan, T. B. Wang, C. F. Gao, X. Z. Lan, Mesoscopic Phase Behavior of Tridecane – Tetradecane Mixtures Confined in Porous Materials: Effects of Pore Size and Pore Geometry, *J. Phys. Chem. C*, **117**, 17245-17255 (2013).

15. P. A. Artola, A. Raihane, C. Crauste-Thibierge, D. Merlet, M. Emo, C. Alba-Simionesco, B. Rousseau, Limit of Miscibility and Nanophase Separation in Associated Mixtures, *J. Phys. Chem. B*, **117**, 9718-9727 (2013).

16. K. Morishige, K. Mikawa, Tensile Effect on Crystal Nucleation of Methanol and Ethanol Confined in Pores, *J. Phys. Chem. C*, **116**, 3618-3622 (2012).

17. L. D. Gelb, K. E. Gubbins, R. Radhakrishnan, M. Sliwinska-Bartkowiak, Phase separation in confined systems, *Rep. Prog. Phys.*, **62**, 1573 (1999).

18. R. Zaleski, W. Dolecki, A. Kierys, J. Goworek, *n*-Heptane adsorption and desorption on porous silica observed by positron annihilation lifetime spectroscopy, *Microporous and Mesoporous Materials*, **154**, 142-147 (2012).

19. S. Srivastava, P Agarwal, L. A. Archer, Tethered Nanoparticle – Polymer Composites: Phase Stability and Curvature, *Langmuir*, **28**, 6276-6281 (2012).

20. M. S. Gruszkiewicz, G. Rother, D. J. Wesolowski, Direct Measurements of Pore Fluid Density by Vibrating Tube Densimetry, *Langmuir*, **28**, 5070-5078 (2012).

21. Y. Wang, P. Keblinski, Effect of interfacial Interactions and nanoscale Confinement on Octane Melting, *J. App. Phys.,* **111,** 064321 (2012).

22. T. Hofmann, D. Wallacher, M. Mayorova, R. Zorn, B. Frick, P. Huber, Molecular Dynamics of n-Hexane: a Quasi-Elastic Neutron Scattering Study on the Bulk and Spatially Nanochannel-Confined Liquid, *preprint server*, arXiv:1204.2362v1 [cond-mat.soft] 11 Apr 2012.

Papers concerning gas solubility in confined solvents:

23. N. L. Ho, F. Porcheron, R. J.-M. Pellenq, Experimental and Molecular Simulation Investigation of Enhanced CO_2 Solubility in Hybrid Adsorbents, *Langmuir*, **26 (16)**, 13287-13296 (2010).

24. A. Luzar, D. Bratko, Gas Solubility in Hydrophobic Confinement, *J. Phys. Chem. B*, **109**, 22545-22552 (2005).

25. L. N. Ho, J. Perez-Pellitero, F. Porcheron, R. J.-M. Pellenq, Enhanced CO_2 Solubility in Hybrid MCM-41: Molecular Simulations and Experiments, *Langmuir*, **27**, 8187-8197 (2011).

26. N. L. Ho, J. Perez-Pellitero, F. Porcheron, R. J.-M. Pellenq, Enhanced CO_2 Solubility in Hybrid Adsorbents: Optimization of Solid Support and Solvent Properties for CO_2 Capture, *J. Phys. Chem. C*, **116**, 3600-3607 (2012).

27. E. Soubeyrand-Lenoir, C. Vagner, J. W. Yoon, P. Bazin, F. Ragon, Y. K. Hwang, C. Serre, J.-S. Chang, P. L. Llewellyn, How Water Fosters a Remarkable 5-Fold Increase in Low-Pressure CO_2 Uptake within Mesoporous MIL-100(Fe), *J. Am. Chem. Soc.*, **134**, 10174-10181 (2012).

28. J. Liu, Y. Zhou, Y. Sun, W. Su, L. Zhou, Methane storage in wet carbon of tailored pore sizes, *Carbon*, **49**, 3731-3736 (2011).

29. L. Mu, B. Liu, H. Liu, Y Yang, C. Sun, G. Chen, A novel method to improve the gas storage capacity of ZIF-8, *J. Mater. Chem.*, **22**, 12246-12252 (2012).

30. D. Zhou, J. Mi, C. Zhong, Theoretical Study of Dissolved Gas at a Hydrophobic Interface, *J. Phys. Chem. C*, **116**, 3042-3049 (2012).

31. Z. K. Lopez-Castillo, S. N. V K. Aki, M. A. Stadtherr, J. F. Brennecke, Enhanced Solubility of Hydrogen in CO_2-Expanded Liquids, *Ind. Eng. Chem. Res.*, **47**, 570-576 (2008).

32. S. Tanaka, K. Kida, H. Fujimoto, T. Makino, Y. Miyake, Self-Assembling Imidazolium-Based Ionic Liquid in Rigid Nanopores Induces Anomalous CO_2 Adsorption at Low Pressure, *Langmuir*, **27**, 7991-7995 (2011).

Papers on porous liquids:

33. N. O'Reilly, N. Giri, S. L. James, Porous Liquids, *Chem. Eur. J.*, **13**, 3020-3025 (2007).

34. J. R. Holst, A. Trewin, A. I. Cooper, Porous organic molecules, *Nature Chemistry*, **Vol. 2**, 915-920 (2010).

35. G. Melaugh, N. Giri, C. E. Davidson, S. L. James, M. G. Del Pópolo, Designing and understanding permanent microporosity in liquids, *Phys. Chem. Chem. Phys.*, **16**, 9422-9431 (2014).

Miscellaneous papers:

36. M. Kaźmierczak, A. Katrusiak, The Most Loose Crystals of Organic Compounds, *J. Phys. Chem. C*, **117**, 1441-1446 (2013).

37. W. Wang, C. Ma, P. Lin, L. Sun, A. I. Cooper, Gas storage in renewable bioclathrates, *Energy Environ. Sci.*, **6**, 105-107 (2013).

38. S. Jiang, J. T. A. Jones, T. Hasell, C. E. Blythe, D. J. Adams, A. Trewin, A. I. Cooper, Porous Organic Molecular Solids by Dynamic Covalent Scrambling, *Nature Commun*., 2:207, DOI:10.1038/ncomms1207 (2011).